

# Global Sensitivity Analysis to Optimize Basin-Scale Conductive Model Calibration – A Case Study From the Upper Rhine Graben

Denise Degen<sup>a,\*</sup>, Karen Veroy<sup>b,c</sup>, Jessica Freyemark<sup>d,e</sup>, Magdalena Scheck-Wenderoth<sup>d,e</sup>, Thomas Poulet<sup>f</sup>, Florian Wellmann<sup>a</sup>

<sup>a</sup>*Computational Geoscience and Reservoir Engineering (CGRE), RWTH Aachen University, Wüllnerstraße 2, 52072 Aachen, Germany*

<sup>b</sup>*Centre for Analysis, Scientific Computing and Applications, Department of Mathematics & Computer Science, Eindhoven University of Technology (TU/e), Groene Loper 5, Eindhoven, The Netherlands*

<sup>c</sup>*Faculty of Civil Engineering, RWTH Aachen University, Schinkelstraße 2, Aachen, Germany*

<sup>d</sup>*GFZ German Research Centre for Geosciences, Telegrafenberg, 14473 Potsdam, Germany*

<sup>e</sup>*Department of Geology, Geochemistry of Petroleum and Coal, RWTH Aachen University, Aachen, Germany*

<sup>f</sup>*CSIRO Mineral Resources, Kensington, Western Australia*

---

## Abstract

Calibrating geothermal simulations is a critical step, both in scientific and industrial contexts, with suitable model parameterizations being optimized to reduce discrepancies between simulated and measured temperatures. Here we present a methodology to identify model errors in the calibration and compensate for measurement sparsity. With an application to the Upper Rhine Graben, we demonstrate the essential need for global sensitivity studies to robustly calibrate geothermal models, showing that local studies overestimate the influence of some parameters. We ensure the feasibility of the study through a physics-based machine learning approach (reduced basis method), reducing computation time by several orders of magnitude.

*Keywords:* global sensitivity analysis, sensitivity-driven model calibration, Upper Rhine Graben, reduced basis method

---

\*Corresponding author

## 1. Introduction

Physics-based forward modeling simulations are used in a wide range of geothermal studies – from the investigation of global and regional temperature fields to local reservoir studies (Cacace et al., 2013; Kolditz & Clauser, 1998; Konrad et al., 2019; Randolph & Saar, 2011). As in many geoscientific applications, these simulations are based on models with associated uncertainties in the selection of the physical model (conductive, hydrothermal, mechanical, etc.), the geological model itself, as well as all relevant parameters (boundary conditions and material properties, including hydraulic and thermal conductivities, radiogenic heat production, etc.). To compensate for these model errors, arising from, for instance, measurement errors, generalizations, and geometrical uncertainties (Houghton et al., 2001; Murphy et al., 2004; Refsgaard et al., 2007; Wellmann & Caumon, 2018), we need an appropriate calibration process.

Reliable and robust model calibrations represent a particular challenge for deep geothermal systems because most temperature measurements come from shallow depth. Typically, only a limited number of deeper measurements are available for the model validation. This imbalance has an important influence on the ability to constrain uncertain model parameters: if a model parameter only has a very limited influence on the output value at the position of the available data points, then, logically, it will be difficult to estimate this parameter from the available data. The analysis of parameters that can be identified and calibrated is the main goal of the field of sensitivity analysis (Saltelli et al., 2004). Here, we investigate the requirement for sensitivity analyses and potential of automated model calibrations for the specific case of regional conductive heat flow models on the basin scale, with an application to the Upper Rhine Graben in Central Europe.

Sensitivity analyses can be categorized into local and global analyses (Saltelli et al., 2004; Wainwright et al., 2014). The local sensitivity analysis (SA) investigates the influence of the model parameters on the model response in the vicinity of the initial parameters. Furthermore, the local SA assumes that the

parameters are independent. As such, local SAs have known deficiencies as they are only locally investigating the first-order parameter influence around a given parameter set. In contrast, the global SA investigates the entire parameter domain and considers parameter correlations. In the work presented here, we investigate both local and global approaches and evaluate specifically the requirement and added value of global SA for regional geothermal simulation studies on the scale of an entire basin (Sobol, 2001; Wainwright et al., 2014).

Global sensitivity analyses in geosciences have been performed for hydrological studies (van Griensven et al., 2006; Tang et al., 2007; Cloke et al., 2008; Zhan et al., 2013; Baroni & Tarantola, 2014; Song et al., 2015), for volcanic source modeling (Cannavó, 2012), and for geothermal heat exchangers (Fernández et al., 2017), to name just a few fields. Furthermore, a comparison of local and global sensitivity analysis has been performed for a hydrological model in Wainwright et al. (2014). However, there is no comparison of local and global sensitivity analyses for basin-scale geothermal heat flow models available yet, as presented here, with a focus also on the uneven distribution of measurement points.

In geothermal applications, the material parameters including thermal conductivities and radiogenic heat productions are usually associated with high uncertainties (Freymark et al., 2017; Lehmann et al., 1998; Vogt et al., 2010; Wagner & Clauser, 2005). These high uncertainties quickly lead to wrong initial guesses of the various parameters, bearing the substantial risk of exploring the wrong part of the parameter space with a local sensitivity analysis. Based on this realization, global SAs have been developed (see Saltelli et al., 2004 for an overview), but these typically require many thousand forward simulations and are therefore often infeasible for more complex or larger simulations, where a single simulation run can require tens of minutes or even hours of simulation time.

To overcome the problem of the long simulation time, and to make global SAs possible for geothermal conductive heat flow models, we apply here the reduced basis (RB) method to obtain a highly efficient surrogate model for the entire

forward simulation. The RB method is essentially a physics-based machine learning approach (Hesthaven et al. 2016; Prud'homme et al. 2002; Quarteroni et al. 2015). This method has been adapted successfully for geophysical simulations (Degen et al. 2020) and showed promising results with a reduction of simulation time by several orders of magnitude, after model training, while still providing highly accurate estimates of state variables at measurement locations. We apply this method here to make a global SA feasible and to efficiently test several model scenarios.

While focusing on the model calibration methodology, our study also derives some new information about the case study of the Upper Rhine Graben and its surrounding region, Central Europe. This region has gained significant interest for deep geothermal exploration due to its high geothermal gradient, for example around Soultz-sous-Forêts, Landau, and Bruchsal (Agemar et al. 2013, 2014; Illies, 1972; Pauwels et al. 1993; Geothermie 2007; Vidal et al. 2015). However, obtaining reliable spatial temperature distributions is a major challenge as seen in the ongoing discussion in the literature (Agemar et al. 2013, 2014; Freyemark et al. 2017, 2019; GeORG-Projektteam 2013; Grimmer et al. 2017; Stober & Bucher 2015), partly because of the unclear influence of advection on the temperature distribution within the Upper Rhine Graben. So far, mostly “trial-and-error” model calibrations have been performed in basin-scale models of this region (e.g. Freyemark et al. 2017). With this work, we aim to contribute with a detailed global SA, followed by a full calibration of a conductive geothermal model, and identify the suitability of such a model in different regions of the basin.

The paper is structured as follows: We provide an overview of the numerical methods, including sensitivity analyses, model calibrations, and the reduced basis method in Section 2. This is followed by a comparison of various model calibrations, considering different sensitivity analysis techniques and different data weighting schemes for the Upper Rhine Graben in Section 3. We discuss the results in Section 4 and present concluding remarks in Section 5.

## 2. Materials and Methods

This section presents the conceptual differences between local and global sensitivity analyses, in order to demonstrate the need for global sensitivity analyses for robust and reliable model calibrations. As stated in the Introduction, our case studies using sensitivity analysis are limited here to thermal basin-scale applications. To focus solely on the methodology, we first perform this comparison on a simplified geological model, even though the results are not restricted to simple models but apply in general, as will be seen in Section 3 with the case study of the Upper Rhine Graben.

### 2.1. Forward Simulation

The first step in a simulation is to select a physical model, which we take as the one for the real-case study of Section 3 to ensure the basic comparison of this section can be directly extended later on. With the focus of this contribution on the methodology, we keep the physics simple and do not consider convection processes, despite their potential importance in the Upper Rhine Graben (Freymark et al. 2019). For the forward simulations of the temperatures, we follow therefore Bayer et al. (1997) and consider a steady-state geothermal heat conduction problem with a radiogenic heat production:

$$\lambda \nabla^2 T + S = 0, \quad (1)$$

where  $\lambda$  is the thermal conductivity,  $T$  the temperature and  $S$  the radiogenic heat production.

We are taking only nondimensional parameters and variables into account, which leads to Eq. 2

$$\frac{\lambda}{\lambda_{\text{ref}} S_{\text{ref}}} \frac{\nabla^2}{l_{\text{ref}}^2} \left( \frac{T - T_{\text{ref}}}{T_{\text{ref}}} \right) + \frac{S}{S_{\text{ref}} T_{\text{ref}} \lambda_{\text{ref}}} = 0 \quad (2)$$

Here,  $\lambda_{\text{ref}}$  is the reference thermal conductivity,  $T_{\text{ref}}$  the reference temperature,  $S_{\text{ref}}$  the reference radiogenic heat production, and  $l_{\text{ref}}$  the reference length. Furthermore, the Laplace operator ( $\nabla$ ) acts on the non-dimensional space.

For all models presented in this paper, we use Dirichlet boundary conditions at the top and base of the model and zero Neumann boundary conditions from all vertical model boundaries.

110 Noting the focus of this paper on the methodology and on large-scale features, we do not account for local spatial heterogeneities of the thermal properties ( $\lambda$ ,  $S$ ). Those parameters, throughout the whole paper, are therefore considered as homogeneous and isotropic, with constant values within each geological layer.

## 115 2.2. Sensitivity Analysis

We now compare the two end-member concepts of local and global sensitivity analysis on the conductive heat transport model presented above, noting that the results extend to other physical problems.

We consider a function  $f$  such that  $u = f(x)$ , with  $x = (x_1, \dots, x_N)$  the model parameters and  $u^* = f(x^*)$  the required solution at the optimal parameter set  $x^*$ . A sensitivity analysis aims to determine the influence of the model parameters  $x$  on the model  $f(x)$  (Sobol 2001; Wainwright et al. 2014), and can be performed locally or globally (Sobol 2001), as discussed in the next sections. In the following, we briefly describe the main difference between both analyses, 125 and illustrate the concepts by using a simplified geological basin-scale model (Fig. 2.1), while keeping the same governing equations as for the subsequent case study.

□ The simple model is derived from the Upper Rhine Graben model (Freymark et al. 2017), extending 292 km in the x-direction, 525 km in the y-direction, 130 and -80 km in the z-direction. The material parameter values are also taken from Freymark et al. (2017), with the top layer corresponding to the Cenozoic Volcanics, the middle layer to the Upper Crust Saxothuringian (consisting of slate and granitoids), and the base layer to the lithospheric mantle. The top boundary condition is 10 °C, which corresponds to the annual average surface 135 temperature in Germany (Deutscher Wetterdienst 2020). The base boundary condition is set to the 1300 °C isotherm since the lower model boundary

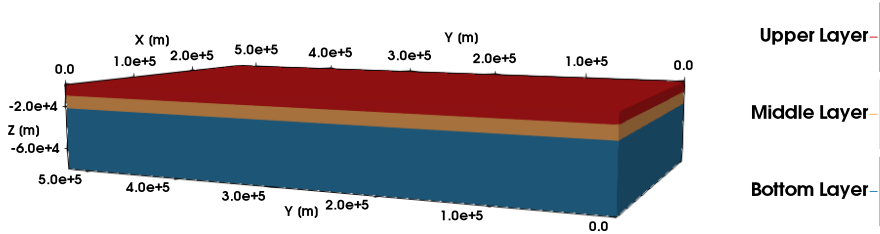


Figure 2.1: Simplified basin-scale model for illustrating the concepts of the methods presented in this chapter.

is assumed to correspond to the thermal lithosphere-asthenosphere boundary (LAB) (Turcotte & Schubert, 2002). Note that we perform all simulations with the nondimensional equation 2 for investigating the relative importance of the model parameters and for efficiency reasons. Hence, we solve for nondimensional temperatures between -1 and 0. Additionally, we apply a lifting function removing the static effects of the lower boundary condition. The lifting function is introduced in equation 10 of Section 3 and required for a efficient performance of all analyses.

We investigate the sensitivities of all thermal conductivities and the radiogenic heat production of the Saxothuringian.

### 2.2.1. Local Sensitivity Analysis

We go back to the generic definition of the function  $u = f(x)$ , with  $x = (x_1, \dots, x_N)$ . Note that  $u$  is a generic function that can contain any value. In our geothermal study a  $u$  typically contains numerous temperature measurements of our model domain. Performing a local sensitivity analysis at  $x^0$  consists in evaluating  $\left(\frac{\partial u}{\partial x_k}\right)_{x=x^0}$ . Hence, the local SA investigates the influence of the various model parameters with respect to a pre-defined reference parameter set  $x^0$ . For this reason, local sensitivity analyses focus on the sensitivity in the vicinity of the input parameters (Sobol, 2001; Wainwright et al., 2014) and they do not consider parameter correlations. They assume that the influence observed for each realization is solely arising from the single changed model

parameter, which itself is allowed a defined maximum variation (e.g., 1 %).

In the case of a geothermal application, we would, for instance, determine  
160 the influence of the different thermal conductivities with respect to a reference  
set, which would usually be our initial guess. That already shows the major  
issue with local sensitivity analyses: defining that reference  $x^0$ . Once selected,  
we evaluate the function  $f$  at that parameter set  $x^0$ , i.e. we calculate the  
reference temperatures at our observation points, using our physical model with  
165 those parameters. Ideally, we would like these reference temperatures to match  
the observed ones, but this is unlikely, if not impossible, due to model and  
measurement errors. Hence, despite naturally using our “best” knowledge as  
the reference, the inherent uncertainties related to geothermal applications lead  
to discrepancy between this “best” knowledge and the “true” parameter values.  
170 Therefore, we introduce an error in the sensitivity analysis that can lead to  
wrong and possibly misleading estimates of parameter sensitivities.

We apply now this process to our simple basin-scale model with a 1% varia-  
tion in parameter values and investigate the influence of the model parameters  
of the simplified model on the absolute misfit between the simulated and the  
175 reference temperature data, for which we use the same data as for the real-case  
model of Section 3. The results are presented in green in Fig. 2.2. We observe  
that the sensitivities are similar for all parameters. If we would compare the  
simulated temperatures to the observed temperatures directly (instead of the  
reference temperatures), we would obtain equal sensitivities for all parameters,  
180 which is due to the fact that these temperatures lie outside the imposed range  
of 1 % variation from the true values. We also note that the response of the  
simplified model is sensitive to all investigated parameters assuming an arbi-  
trary threshold<sup>1</sup> of  $10^{-1}$  (shown as a black line in Fig. 2.2). This means that we  
would have to consider all model parameters of the simplified model for further

---

<sup>1</sup>Note that it is not possible to define a general value for the threshold because it depends on what we consider as “sensitive”. This might differ from application to application. In this paper, we look for a significant drop in the sensitivity index values to define the threshold.

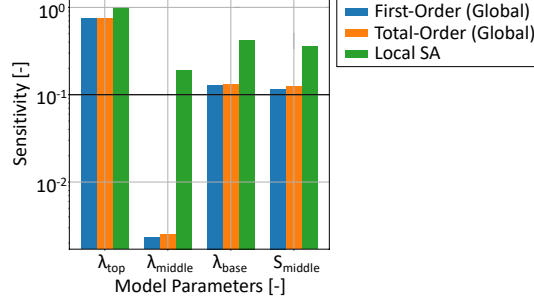


Figure 2.2: Local and global sensitivity analysis for the benchmark problem.

185 analyses.

### 2.2.2. Global Sensitivity Analysis

For the global analysis, the idea is to remove the constraint of the reference  $x^0$ . In this paper, we use the Sobol sensitivity analysis with the Saltelli sampler as our global method. The Sobol sensitivity analysis is a variance-based method (Sobol 2001; Saltelli 2002; Saltelli et al. 2010; Wainwright et al. 2014). It does not set  $x = x^0$ , but evaluates instead the entire model  $f(x)$ . Assuming a square-integrable function with orthogonal members, we can decompose it into the following form (Sobol 2001):

$$\int f^2(x)dx - f_0^2 = \sum_{s=1}^n \sum_{i_1 < \dots < i_s} \int f_{i_1 \dots i_s}^2 dx_{i_1} \dots dx_{i_s}, \quad (3)$$

where  $1 \leq i_1 < \dots < i_s \leq n$ ,  $f_0$  is a constant, and  $f_i$  a function. Eq. 3 can be rewritten as:

$$\int f^2(x)dx - f_0^2 = \sum_i \int f_i^2(x_i) + \sum_{i < j} \int f_{ij}^2(x_i, x_j) + \dots + \int f_{12 \dots n}^2(x_1, x_2, \dots, x_n). \quad (4)$$

The variances  $D$  are then defined as (Sobol 2001):

$$D = \int f^2 dx - f_0^2, \quad D_{i_1 \dots i_s} = \int f_{i_1 \dots i_s}^2 dx_{i_1} \dots dx_{i_s}. \quad (5)$$

The global sensitivity indices  $S$  can be derived from the variances by taking the ratio (Sobol 2001):

$$S_{i_1 \dots i_s} = \frac{D_{i_1 \dots i_s}}{D}. \quad (6)$$

This means that the Sobol sensitivity index is defined as the ratio between the partial and total variance.

We use the global sensitivity analyses to investigate the influence of the model parameters on the total absolute misfit between the simulated and the observed temperature data. In contrast to the local SA, the global SA does not require a reference and investigates the influences of all parameters within the pre-defined parameter ranges (Sobol 2001). Hence, we are no longer restricted to small parameter variations. Furthermore, we no longer need to know the parameter distribution in advance and only specify an allowable physical range.

The first-order index represents the influence of the model parameter on the model itself. The second-order index describes the influence of the correlation between two parameters. Further, higher-order indices are available to investigate the influence of the correlation between more than two parameters (Sobol 2001). For further details regarding the definition of the sensitivity indices, we refer to Sobol (2001), and for further information regarding the sampling procedure, we refer to Saltelli (2002), and Saltelli et al. (2010).

In the example of the geothermal simulation considered here, we no longer need to specify our (actually wrong) “best” knowledge of the thermal properties. We performed the global sensitivity analysis for the simple basin-scale model (Fig. 2.2), using 10,000 realizations per parameter to reduce the statistical error and eliminate negative sensitivities, yielding a computationally extremely demanding analysis of in total 100,000 forward solves. To compensate for this high computational cost, we construct a fast, physics-preserving, and highly accurate surrogate model. The sensitivity analysis is executed using the Python library SALib (Herman & Usher, 2017). The results, of the first-order indices (shown in blue) and the total-order indices (shown in orange) in Fig. 2.2, differ significantly from those of the local sensitivity analysis (in green). We still observe the dominant influence of the thermal conductivity of the top layer; however, we see that the model response is insensitive to the thermal conductivity of the middle layer. This means that the local sensitivity analysis overestimates the influence of this particular model parameter. Furthermore, the local analysis

overestimates the influence of both the thermal conductivity of the base layer and the radiogenic heat production of the middle layer. In contrast to the local SA, the results of the global SA allow us to reduce the dimension of the parameter space from four to three.

In addition to the total sensitivities, we obtain information about the parameter correlations. For the presented model, we observe nearly exclusive first-order contributions. Hence, the parameter correlations in the presented model are small. This could be seen as an argument to claim that the local SA should be ideally suited for this model; yet it clearly fails. Conversely, the global SA has a different issue, requiring many forward simulations. In Section 3, we describe how we overcome this disadvantage.

### 2.3. Model Calibration

Based on the results of the sensitivity study, we perform model calibrations on the most relevant parameters only, i.e. those whose sensitivity is above the selected threshold of  $10^{-1}$ . Hence, the sensitivity analysis is a natural preparation step for a model calibration (Ray et al., 2015). As we demonstrate in this paper, the efficient reduction of the parameter space leads to more robust model calibration results.

We use the trust region reflective (TRF) method from SciPy (Branch et al., 1999; Jones et al., 2014) as our calibration method since it is robust and considers bounds for the model parameters (Jones et al., 2014). Especially the latter aspect is actually of utmost importance since our surrogate models are only valid if we remain within the pre-defined training ranges. This is the reason why we cannot use, for instance, the conjugate gradient method provided by SciPy, whose implementation does not allow the consideration of bounds for the model parameters.

Take the following problem into account:  $\min_{x \in \mathbb{R}^n} \{m(x) : l \leq x \leq u\}$ , where we want to minimize the function  $m(x)$  with  $x$  being our model parameter. Furthermore, the model parameters are bounded below by the lower bound  $l$ , and above by the upper bound  $u$ . The method defines a trust region  $N$  around

the current “best” solution to improve the convergence rate. In standard trust  
 region methods, the quadratic model  $q(s)$  is assumed to approximate the orig-  
 250 inal objective function inside the trust region. We derive the quadratic model  
 by taking the first two steps of the Taylor expansion of  $m$  at  $x$ . The trial  
 step  $s$  is computed by minimizing over the trust region:  $\min_s \{q(s), s \in N\}$ .  
 The current point is updated to  $x + s$  if  $m(x + s) < m(x)$  and the trust re-  
 gion is updated. If we do not fulfill this condition, the current point stays  
 255 the same. Then, we decrease the trust region and repeat the computation of  
 the trial step. The trust region optimization problem is then expressed as:  
 $\min \{ \frac{1}{2} s^T H s + s^T g \text{ such that } \|Ds\| \leq \Delta \}$ . Here,  $g$  is the gradient,  $H$  the Hes-  
 sian matrix,  $D$  a diagonal scaling matrix, and  $\Delta$  a positive scalar. We repeat  
 these steps until we reach convergence. Minimizing a quadratic function – in-  
 260 stead of the original, possibly non-linear, objective function – results in a re-  
 duction in computation time. More details about the method can be found in  
[Branch et al. \(1999\)](#).

### 3. Case Study of the Upper Rhine Graben

After illustrating the shortcomings of a local sensitivity analysis for our  
 265 simple basin-scale model, we extend the study to the real-case study of the  
 Upper Rhine Graben, presented in [Freymark et al. \(2017\)](#). As mentioned in  
 the introduction, our purpose is not to discuss the assumptions and validity of  
 this particular geological model but to demonstrate the impact of global SAs  
 on a given study. Furthermore, we demonstrate the consequences of the out-  
 270 come of the sensitivity analysis for further analyses such as model calibrations.  
 First, we introduce both the high-dimensional finite element (FE) and the low-  
 dimensional RB model and then we present the results for the sensitivity-driven  
 model calibrations. Fig. [3.3](#) summarises all model scenarios used for the model  
 calibrations and sensitivity analyses of this Upper Rhine Graben case study.

275 3.1. Upper Rhine Graben – High-Dimensional Model

Our study is based on the model of the Upper Rhine Graben presented in Freymark et al. (2017), which is solved using the FE method. This approach explicitly simulates the whole problem and is therefore referred to as the high dimensional model. We recall here some of its numerical aspects for convenience.

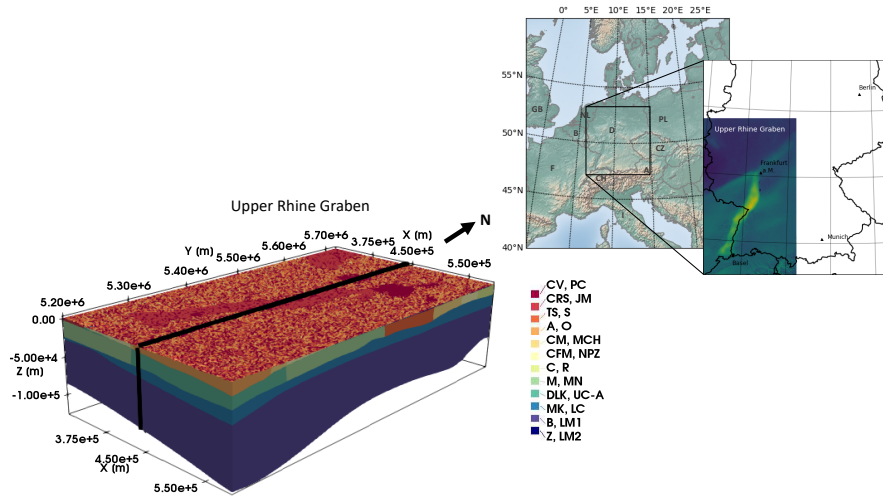


Figure 3.1: Geology of the Upper Rhine Graben. The cross-section that is later used for visualizing the sensitivities is indicated by a black line. The acronyms for the respective geological layers are defined in Tab. 1 in the Supplementary Material. In the upper left corner, we show the location of the model.

280 The 3D model (Fig. 3.1) extends 292 km in the  $x$ -direction, 525 km in the  $y$ -direction, and in the vertical direction down to the lithosphere-asthenosphere boundary. It consists of 24 geological units and is discretized using deformed eight-noded prisms. The horizontal resolution is one km, and the vertical resolution corresponds to the layer thickness yielding 3,852,950 degrees of freedom.

285 At the top and base of the model, we apply Dirichlet boundary conditions. We set all lateral boundaries to no-flow boundaries. For the upper boundary condition, we use the annual average surface temperatures, as presented in Freymark et al. (2017). In contrast, the lower boundary condition is the 1300 °C isotherm at the LAB (Turcotte & Schubert 2002).

### 290 3.2. Data and Weighting

The temperature sampling points used for calibration are very unequally distributed throughout the spatial domain. To compensate for this inequality, we introduce weights. For the calculation of the weights, we consider two methods: first, we calculate them automatically via a distance matrix provided by SciPy, and second, we specify them via user-input. Both weighting schemes are displayed in a map view in Fig. 3.2. We obtain the user-defined weighting by splitting the data into three regions (Fig. 3.2). The decision of subdividing the data into three different regions is made upon their depth distribution and the underlying physical behavior. In detail, region 3 contains the data points below -2,5 km. Region 2, contains the data points deviating from the trend that a conductive model introduces. All remaining points are associated to region 1. We note that region 3, which corresponds to the northern part of the Upper Rhine Graben, contains only a few points. To compensate for its data sparsity, we apply a weight of 10 to the misfit in this region. We also note that many observation data are available in the Hesse area (northeast of Frankfurt a. M. in Fig. 3.2) while significantly fewer data are available for the Upper Rhine Graben (gray outline, labeled with URG). To compensate for this unequal data distribution, we apply a weight of 0.1 to region 1 and 1.0 to region 2. To explain the assigned weights for region 1 to 3, we have 2282 data points in region 1, 53 in region 2, and 12 data points in region 3 (Fig. 3.1). Hence, region 1 contains one order of magnitude more data than region 2 (resulting in the weight of 0.1 for region 1) and two orders of magnitude more data than region 3 (yielding the weight of 10 in region 3).

### 3.3. Upper Rhine Graben – Low-Dimensional Model

315 Based on the full FE model, we constructed two reduced models:

- The first reduced model (branch 1 of Fig. 3.3) considers only thermal conductivities as model parameters. It consists of 12 different parameters since we combined those layers with equal thermal conductivities.

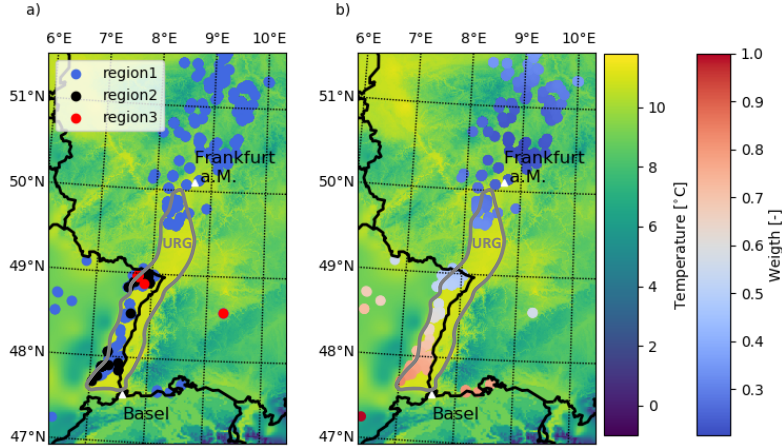


Figure 3.2: Distribution of weights for automated model calibration, showing the a) user-defined and b) automatic weights. The user-defined weights are derived from expert knowledge, and the automatic weights by using the distance matrix. In the background of all images are the annual regional average surface temperature values plotted. The gray line indicates the main outline of the Upper Rhine Graben. Note that region 1 has a weight of 0.1, region 2 of 1.0, and region 3 of 10.0.

- The second reduced model (branch 2 of Fig. 3.3) contains the thermal conductivity of the Cenozoic Rift Sediments and the radiogenic heat productions from the Upper Crust, resulting in eight parameters.

In both models, we take the allowed parameters ranges from Freymark et al. (2017). If no range is provided, we allow a variation of  $\pm 50\%$  from the initial value. For the nondimensional representation of the problem, we set the reference thermal conductivity  $\lambda_{\text{ref}}$  to the maximum thermal conductivity of  $6.0 \text{ W m}^{-1} \text{ K}^{-1}$ . We choose the maximum temperature of  $1300 \text{ }^\circ\text{C}$  as the reference temperature  $T_{\text{ref}}$  and the maximum radiogenic heat production of  $3.0 \text{ } \mu\text{W m}^3$  as the reference radiogenic heat production  $S_{\text{ref}}$ . The reference length corresponds to the maximum  $y$ -extent of the mesh (525,000 m).

We use the RB solution as a surrogate model for the FE method. To apply the method, we must decompose the PDE into its parameter-dependent and -

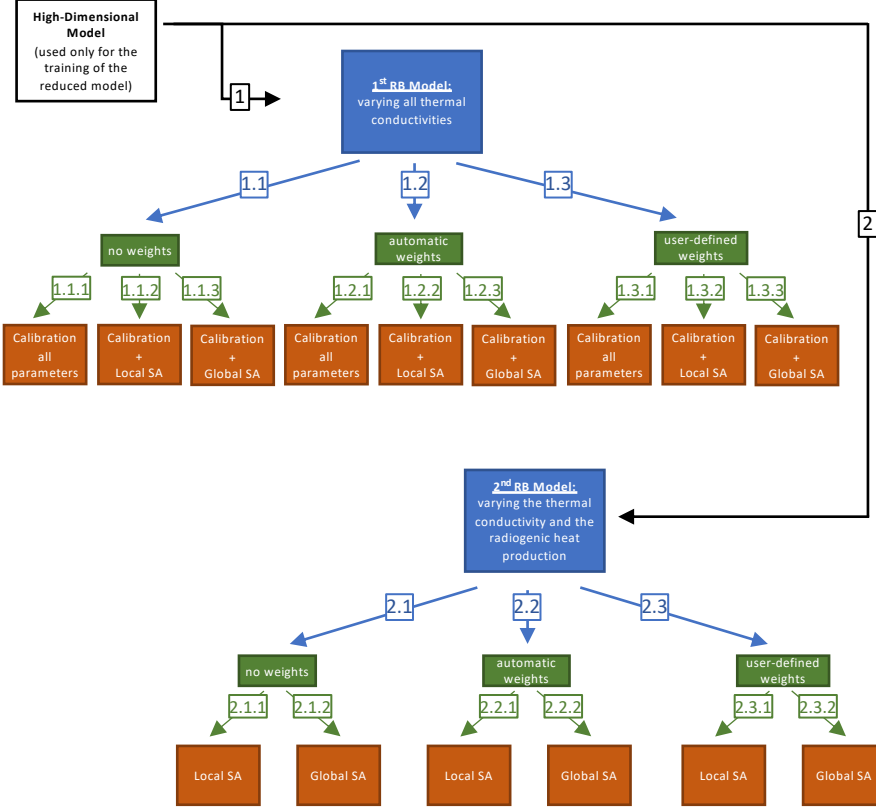


Figure 3.3: Overview of the various model scenarios used for the model calibrations and sensitivity analyses of the Upper Rhine Graben.

independent parts. Within the integral formulation of the problem, we have the stiffness matrix and the load vector. Here, we use the operator representation (equation [7](#)). Therefore, we talk about the bilinear form  $a$  (instead of the stiffness matrix) and the linear form  $l$  (instead of the load vector):

$$a(u(\mu), v; \mu) = l(v; \mu), \quad \forall v \in X, \quad (7)$$

where  $u \in H_0^1(\Omega)$  is the solution,  $\mu \in \mathcal{D}$  the parameter (where  $P =$  the number of parameters),  $v \in X$  the test function,  $X$  the function space ( $H_0^1(\Omega) \subset X \subset H_1(\Omega)$ ), and  $\Omega$  the spatial domain in  $\mathbb{R}^3$ . The decomposition of the bilinear

form  $a$  for both reduced models is given by:

$$a(w, v; \lambda) = \sum_{q=0}^n \lambda_q \int_{\Omega} \nabla w \nabla v \, d\Omega, \quad \forall v, w \in X, \forall \lambda \in \mathcal{D}. \quad (8)$$

330 Here,  $w \in X$  is the trial function, the index “ $q$ ” denotes the number of the training parameters (see also Tab. 1 – 3 in the Supplementary Material), and  $\mathcal{D}$  the parameter domain in  $\mathbb{R}^{12}$ . For the reduced model with varying thermal conductivities (branch 1 of Fig. 3.3),  $n$  is equal to 11, and for the one with varying thermal conductivities and radiogenic heat production (branch 2 of Fig. 3.3),  $n$  is equal to one.

335 The decomposed linear form  $l$  has the following form for the first reduced model (branch 1 of Fig. 3.3):

$$l(v; \lambda) = \sum_{q=0}^n \lambda_q \int_{\Gamma} \nabla v \, g(x, y, z) \, d\Gamma + \int_{\Gamma} \nabla v \, S \, d\Gamma, \quad \forall v \in X, \forall \lambda \in \mathcal{D},$$

with  $g(x, y, z) = T_{\text{top}} \frac{h(x, y, z) - z_{\text{base}}(x, y)}{d(x, y)}$ ,

(9)

where  $\Gamma$  is the domain boundary in  $\mathbb{R}^3$ ,  $n$  is equal to 11,  $g(x, y, z)$  the lifting function,  $T_{\text{top}}$  the temperature at the top of the model,  $h(x, y, z)$  the location in the model,  $z_{\text{base}}(x, y)$  the depth of the base surface, and  $d(x, y)$  the distance between the base and top surface.

The decomposition of the linear form of the second reduced model (branch 2 of Fig. 3.3) is similar:

$$l(v; \lambda) = \int_{\Gamma} \lambda_{(1)} \nabla v \, g(x, y, z) \, d\Gamma + \lambda_1 \int_{\Gamma} \nabla v \, g(x, y, z) +$$

$$d\Gamma \int_{\Gamma} \nabla v \, S_{(14-20)} \, d\Gamma + \sum_{q=14}^n S_q \int_{\Gamma} \nabla v \, d\Gamma, \quad \forall v \in X, \forall \lambda \in \mathcal{D},$$

with  $g(x, y, z) = T_{\text{top}} \frac{h(x, y, z) - z_{\text{base}}(x, y)}{d(x, y)}$ .

(10)

340 Here,  $\lambda_{(1)}$  are all thermal conductivities except the thermal conductivity of the Cenozoic Rift Sediment,  $\lambda_1$  the thermal conductivity of the Cenozoic Rift Sediments,  $S_{14-20}$  the radiogenic heat productions of the upper crust layers, and

$S_{(14-20)}$  all remaining radiogenic heat productions. Furthermore,  $n$  is equal to 20.

#### 345 3.4. Sensitivity-Driven Model Calibration

We present now, for comparison, the model calibration results obtained with three different approaches:

1. A model calibration without a sensitivity analysis,
2. A model calibration with a local sensitivity analysis, and
- 350 3. A model calibration with a global sensitivity analysis.

The first approach is only executed for the first reduced model, whereas the second and third approaches are executed for both reduced model versions. We perform all analyses with all three weighting schemes, which results in a total number of 15 analyses, shown schematically in Fig. 3.3. Note that we only vary  
355 the thermal conductivities for all calibrations of branch of Fig. 3.3 since the influence of the radiogenic heat production is ultimately found to be negligible in comparison to the thermal conductivity, as demonstrated in the following sections.

Some numerical parameters must be defined, which are explained in more  
360 detail in Byrd et al. (1988); Branch et al. (1999); Jones et al. (2014). Within an optimization problem (such as model calibration), we seek to minimize the loss function, which is also referred to as cost function (Golberg 1989; Geem 2012). Here, we use the smooth approximation of the L1 absolute value loss with a value of 0.1 for the soft margin between inlier and outlier residuals to but less  
365 weight on possible outliers. We set the tolerances for the termination to  $10^{-5}$  for changes of the cost function,  $10^{-8}$  for the norm of the gradient, and  $10^{-5}$  for changes of the independent parameters.

Furthermore, note that all forward simulations throughout all model calibrations and sensitivity analyses are performed with the reduced model to speed-up  
370 the analysis time and to make the global sensitivity study feasible.

### 3.4.1. Model Calibration without Sensitivity Analysis

If we do not incorporate any sensitivity result into the model calibration, we consequently have to calibrate our model with all thermal conductivities (branches 1.1.1, 1.2.1, and 1.3.1 of Fig. 3.3). As a reminder, we perform this analysis only for the first reduced model. Tab. 1 (in the Supplementary Material) summarizes the parameter values used as initial guesses and obtained after calibration for all considered scenarios. It is found in the Supplementary Material as it is not the exact values that are important, but the differences between all approaches, which are presented here. The results from the model calibration without weights (branch 1.1.1 of Fig. 3.3) and the model calibration with automatic weights (branch 1.2.1 of Fig. 3.3) are very similar. However, significant differences are observed for the model calibration with user-defined weights (branch 1.3.1 of Fig. 3.3), especially in those four regions: the Cenozoic Volcanics (CV) and Rift Sediments (CRS), and the Lithospheric Mantle (LM1 & LM2)<sup>2</sup>. The difference is particularly pronounced for the CV and CRS regions, where the values of thermal conductivity end up smaller than the initial guess for the model calibration with user-defined weights, yet larger than the initial guess with the other two methods (Tab. 1 in the Supplementary Material).

Furthermore, for all three versions of the model calibration (branches 1.1.1, 1.2.1, and 1.3.1 of Fig. 3.3), many of the calibrated model parameters reach the upper or lower bound of their pre-defined variation range, as shown in Tab. 1 (in the Supplementary Material), indicating that no satisfactory calibration was actually obtained for those parameters within the imposed ranges.

### 3.4.2. Model Calibration with Local Sensitivity Analysis

In this section, we investigate the model calibration of the Upper Rhine Graben under consideration of a local SA. Again, we take all three model weighting versions into account (branches 1.1.2, 1.2.2, and 1.3.2 of Fig. 3.3). First,

---

<sup>2</sup>Note that the separation of the Lithospheric Mantle in Tab. 1 to 3 (in the Supplementary Material) is made to provide a compatibility with Freymark et al. (2017).

we present the sensitivity results, and then we show how to incorporate these results into the model calibration procedure.

400 *Sensitivity Analysis:*

The sensitivity indices resulting from the local sensitivity analyses are shown in Fig. 3.4 for all weighting schemes. In Fig. 3.5, we display them in a cross-sectional view to provide a spatial impression of the distribution of the sensitivities.

405 The local sensitivity analysis without weights (for the reduced model with varying thermal conductivities – branch 1.1.2 of Fig. 3.3) shows influences from the thermal conductivities of the following layers (in descending order):

1. Cenozoic Rift Sediments (CRS) and the Lithospheric Mantle (LM1 & LM2),
- 410 2. Cenozoic Folded Molasse (CM), Cenozoic Foreland Molasse (CFM), Buntsandstein (B)/Jura Mountains (JM), Odenwald (O),
3. Malm (M), Northern Phyllite Zone (NPZ), Rhenohercynian (R), the Mid-German Crystalline High (MCH), and the Lower Crust (LC), and
4. Cenozoic Volcanics (CV).

415 The model response has a sensitivity below 0.1 for the remaining layers. Therefore, we do not consider them for further analyses.

The results for the sensitivity analysis with automatic weights branch 1.2.2 of Fig. 3.3 are similar except that the temperature distribution is also insensitive to the thermal conductivity of the Cenozoic Volcanics (CV). For the analyses with user-defined weights (branch 1.3.2 of Fig. 3.3), we also lose the influence of the Malm (M)/Northern Phyllite Zone (NPZ)/Rhenohercynian (R) layers.

425 For the local sensitivity analysis, using the reduced model with varying thermal conductivity and radiogenic heat production rates (branches 2.1.1, 2.2.1, and 2.3.1 of Fig. 3.3, and Fig. 1 in the Supplementary Material), we see again that the highest impact is arising from the thermal conductivity of the Cenozoic Rift Sediments (CRS). The influences from the radiogenic heat productions of

the upper crust are significantly lower. These results are independent of the weighting scheme.

The results indicate overall a small influence of the radiogenic heat production, which is subsequently disregarded. Therefore, we will not further discuss the second reduced model in this context, but further details can be found in the Supplementary Material.

*Model Calibration:*

Using a cut-off value of  $10^{-1}$  on those local SA results helps reducing the parameter space. For the model calibration with user-defined weights (branch 1.3.2 of Fig. 3.3), the number of parameters drops from twelve to six parameters. The model calibration with automatic weights now only requires seven parameters (branch 1.2.2 of Fig. 3.3) and the model calibration without weights (branch 1.1.2 of Fig. 3.3) eight parameters instead of twelve.

The model calibration results for all calibrated thermal conductivities are shown in details in the Supplementary Material (Tab. 2). The main conclusion is that they are very similar to those obtained by the model calibration with all parameters. Only for the Lower Crust (LC) and the Lithospheric Mantle (LM1 & LM2) do we observe significant differences. We still note that many of the model parameters reach their upper or lower bound, indicating once again that no satisfactory calibration was actually obtained for those parameters within the imposed ranges.

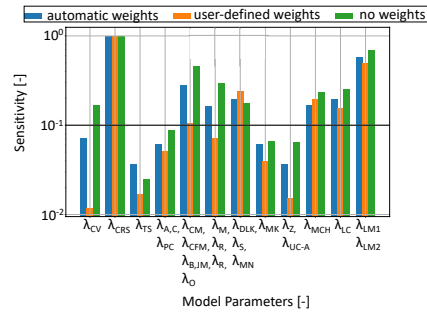


Figure 3.4: Local sensitivity analysis for the reduced order model varying only the thermal conductivities. The acronyms for the respective geological layers are defined in Tab. 1 in the Supplementary Material.

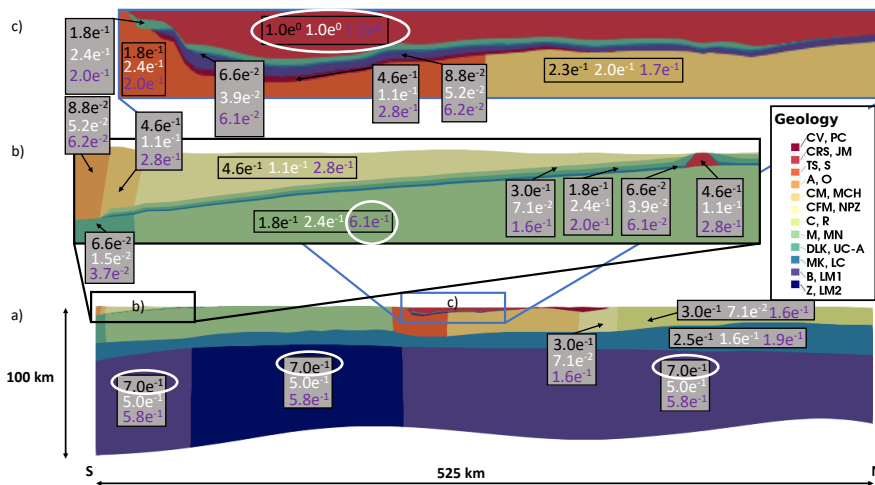


Figure 3.5: Cross-section of the Upper Rhine Graben with the local sensitivities of the different geological layers. The position of the cross-section is highlighted by a black line in Fig. 3.1. The local sensitivities without considering weights are denoted in black, the ones with user-defined weights in white, and the ones with automatic weights in purple. The acronyms for the respective geological layers are defined in Tab. 1 in the Supplementary Material.

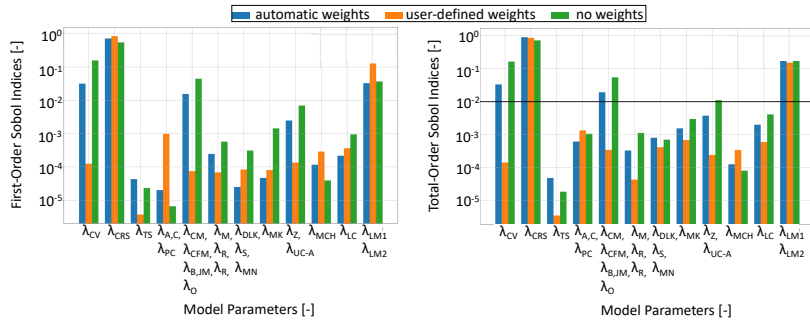


Figure 3.6: Comparison of the first and total order sensitivity-indices of the global sensitivity analyses for the first reduced model of the Upper Rhine Graben model. The acronyms for the respective geological layers are defined in Tab. 1 in the Supplementary Material.

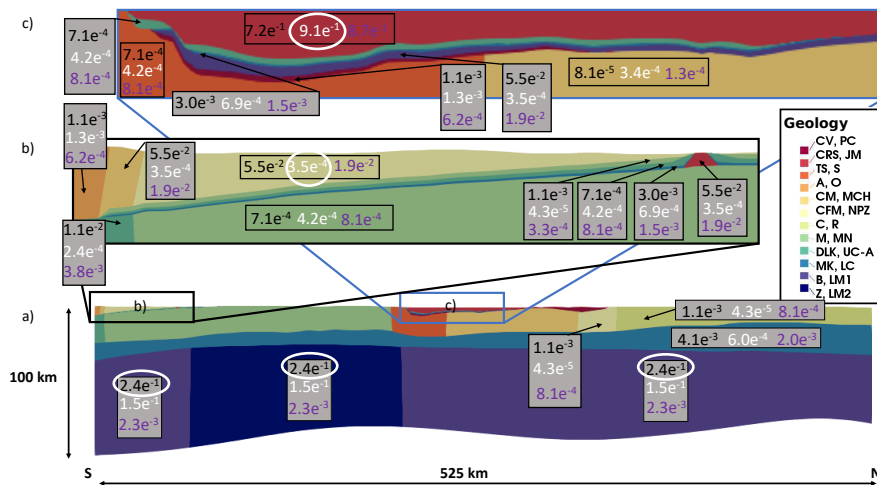


Figure 3.7: Cross-section of the Upper Rhine Graben with the global sensitivities of the different geological layers. The global sensitivities without considering weights are denoted in black, the ones with user-defined weights in white, and the ones with automatic weights in purple. The acronyms for the respective geological layers are defined in Tab. 1 in the Supplementary Material.

### 3.4.3. Model Calibration with Global Sensitivity Analysis

We present now the results from the global SA and the model calibration  
450 using these sensitivity results. Again, we perform all analyses for the scenarios,  
using i) no weights, ii) automatic weights, and iii) user-defined weights.

#### *Sensitivity Analysis:*

For both the sensitivity analysis without weights (branch 1.1.3 of Fig. 3.3) and  
automatic weights (branch 1.2.3 of Fig. 3.3), we obtain similar results. The  
455 first- and total-order indices of the Sobol sensitivity analysis are shown in Fig.  
3.6. Again, we provide the cross-sectional view in Fig. 3.7 to give a spatial  
impression of the sensitivity distribution. The global sensitivity analyses show  
influences of the thermal conductivities of the following layers (in descending  
order):

- 460 1. Cenozoic Rift Sediments (CRS),
2. Cenozoic Volcanics (CV),
3. Lithospheric Mantle (LM1 & LM2), and
4. Cenozoic Folded Molasse (CM), Cenozoic Foreland Molasse (CFM), Bunt-  
sandstein (B), Jura Mountains (JM), Odenwald (O) layers.

465 The influences from all remaining layers are negligible with sensitivities less than  
 $10^{-2}$ . As for the local sensitivity analysis also the influence of the radiogenic heat  
production is negligible.

In addition to the sensitivities for each parameter, we now also obtain an indi-  
cation of higher-order contributions (see Section 2.2.2), which can be attributed  
470 to parameter correlations. The sensitivities are dominated by first-order contri-  
butions for all layers except the Lithospheric Mantle (LM1 & LM2) which also  
has significant higher-order contributions. The Sobol sensitivity analysis with  
user-defined weights (branch 1.3.3 of Fig. 3.3) results in a slightly different pat-  
tern. For this scenario, the higher-order contributions are nearly non-existent  
475 for all layers. Furthermore, we lose the influences of the remaining layers.

#### *Model Calibration:*

For the calibration, we now consider only the thermal conductivities (branches 1.1.3, 1.2.3, and 1.3.3 of Fig. 3.3) since the Sobol sensitivity analysis showed that the influence of the radiogenic heat production is small in comparison to the thermal conductivity. As before, we repeat the calibration in three scenarios. In the no weight and automatic weight scenario (branches 1.1.3, and 1.2.3 of Fig. 3.3), we calibrate with only four instead of 12 parameters. These four parameters are the thermal conductivities of the:

- Cenozoic Volcanics (CV),
- Cenozoic Rift Sediments (CRS),
- Cenozoic Foreland Molasse (CFM), Buntsandstein (B), Jura Mountains (JM), Odenwald (O), and
- Lithospheric Mantle (LM1 & LM2).

The global sensitivity analysis revealed that the model response is insensitive to the other eight parameters. For the case with user-defined weights (branch 1.3.3 of Fig. 3.3), we consider only two parameters (Cenozoic Rift Sediments, CRS, and Lithospheric Mantle, LM1 & LM2).

In Fig. 3.8 we plot the spatial distribution of the user-defined weights. Additionally, we show the misfit between the simulated and observed temperatures for the calibration without weights, with user-defined weights, and for the initial distribution. The misfit between observed and simulated temperatures has its highest values for all realizations in the area of the Upper Rhine Graben (Fig. 3.8). Within the Upper Rhine Graben, the highest misfits are in regions 2 and 3.

Regarding the thermal conductivities, the highest differences between calibrated and uncalibrated values are observed for the Cenozoic Rift Sediments and the Lithospheric Mantle. Note that in contrast to the previous model calibration, we do not reach the bounds of any thermal parameter, which indicates that all parameter got calibrated satisfactorily.

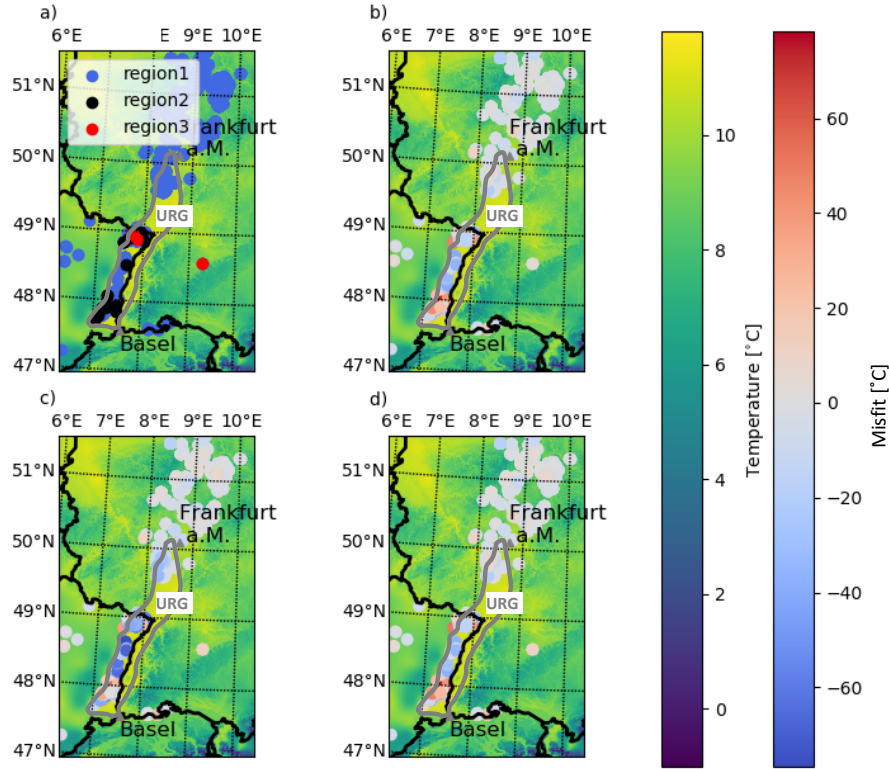


Figure 3.8: Spatial distribution of a) the user-defined weights b) the misfit in temperature for the calibration without weights c) the misfit in temperature after the calibration with user-defined weights, and d) the misfit in temperature for the initial parameter distribution. In the background of all images are the annual regional average surface temperature values plotted. The gray line indicates the main outline of the Upper Rhine Graben.

### 505 3.5. Computational Cost

The reduction requires 128 basis functions to describe the model for a relative error tolerance of  $5 \cdot 10^{-4}$  for the Upper Rhine Graben model, where we vary only the thermal conductivities (Tab. 1 branch 1 of Fig. 3.3). The convergence rate of the maximum relative error bound for both reduced model is shown in Fig. 3.9 We can then reduce the computation time of a single forward simulation from 44 min to 3 ms, yielding a speed-up of  $9.2 \cdot 10^5$ . For the model with a

Table 1: Overview of the computational costs for both reduced models of the Upper Rhine Graben. Here, the first RB model refers to branch 1 in Fig. 3.3 and the second RB model to branch 2 in Fig. 3.3

Model	FE simulation time [s]	Number of basis functions	Online time [s]	Speed-up
First RB model	2,640	128	0.003	$9.2 \cdot 10^5$
Second RB model	2,640	25	0.001	$2.7 \cdot 10^6$

varying thermal conductivity of the Cenozoic Rift Sediments and the varying radiogenic heat productions of the Upper Crust (Tab. 1 branch 2 of Fig. 3.3), 25 basis functions are required to reach an error tolerance of  $1 \cdot 10^{-5}$ . Here, we reduce the computation time to 1 ms, resulting in a speed-up of  $2.7 \cdot 10^6$ .

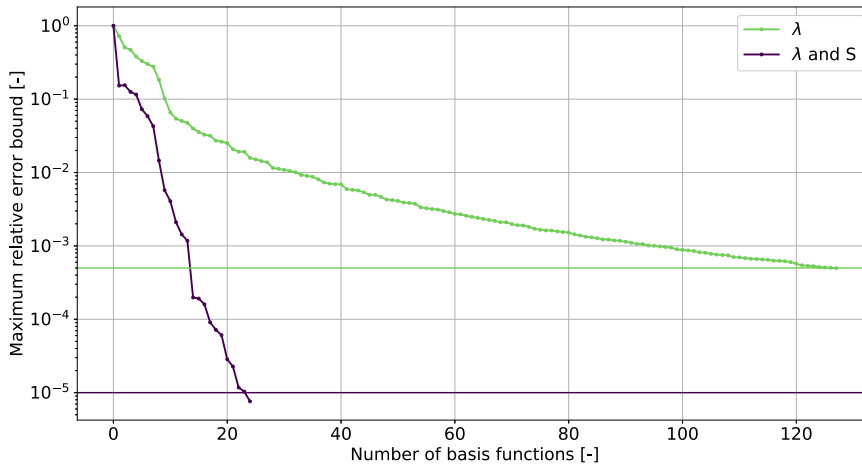


Figure 3.9: Convergence of the relative maximum error bound for both reduced order models. The error bound is relative to the approximation of the “truth” (FE solution). For that reason, it is a measure of the approximation quality.

515

Regarding the cost for the analyses, the global sensitivity analyses required in total 260,000 function evaluations each yielding an execution time of under

500 s. The calibrations require at most seven function evaluations, resulting in a computation time of under 100 ms.

## 520 4. Discussion

The results of our case study highlight the essential need for global sensitivity analyses, required to obtain meaningful, comprehensive, and robust geothermal model calibrations. This aspect is specifically relevant in comparison to traditional “trial-and-error” model calibrations, which we discuss in this section in  
525 more detail. Additionally, we discuss important aspects related to data sparsity and the computational cost of using the RB method instead of the classical FE method.

### *4.1. Local vs. Global Sensitivity Analysis*

Global and local sensitivity analysis both allow to identify parameters that  
530 do not influence the model, leading to a reduction of the number of parameters to consider in further analyses. The quality of the results, though, differs strongly from one method to the other. The common use of local SAs stems from the computational cost of global SAs, which, despite being recognised as a better strategy, certainly appears as prohibitive, at least in absence of any specific  
535 strategy to palliate the fact that forward simulations take minutes to hours to run. This second-best nature of local SAs, however, has been perceived as unimportant until now, most probably since local SAs has provided nonetheless a way for modellers to optimise parameters. To assess the accuracy of this optimisation, we have a closer look at the calibrated parameters from our case  
540 study of Section 3

Many of the calibrated parameters obtained without a SA or with a local SA yield unphysical parameter values (e.g. see Section 3.4.1 and 3.4.2) or reach their arbitrarily imposed bounds (see Tab. 1 and 2 in the Supplementary Material). While a local SA allows to reduce the number of parameters from twelve to  
545 six, seven, or eight parameters depending on the weighting, nonetheless, many

parameters are still reaching their pre-defined bounds. This either shows that:  
i) the bounds were not placed far enough away from the initial parameter distribution, or ii) the parameters are insensitive to the temperature distribution and that consequently the calibration results are meaningless. This is potentially  
550 problematic. Considering the already quite large variation range in our study (up to  $\pm 50\%$ ), the second option is more likely. In such a case of insensitive parameters, the model calibration will fail to correctly determine the best parameter values since all of them result in similar temperature distributions. If we then wanted to perform predictions away from known observations, we  
555 would likely obtain biased and overfitted results.

In contrast to the local SA, no calibrated parameter obtained with the global sensitivity study reaches its bound (see Tab. 3 in the Supplementary Material), independent of the weighting. This points to the robust and reliable results of the global approach, which provides the only way to reduce the parameter space  
560 in an efficient manner. By evaluating the entire parameter space, it provides a way to identify areas of the 3D model where either measurement errors or the underlying physical model itself prevent a suitable match of the observed temperature distribution. The global SA provides both first-order and higher-order sensitivities, i.e. extra information about parameter correlation and additional  
565 insight into the model structure. For instance, the thermal conductivity of the Lithospheric Mantle (LM1 & LM2) is shown to have some influence on other parameters (see Section 3.4.3). In this particular case study, though, we mostly observe first-order contributions and small parameter correlations. This actually makes this study a favourable case for local SAs, which assumes parameter  
570 independence, and only reinforces the superiority of the global approach. Indeed, even in that supposedly advantageous scenario, the local SA results display important shortcomings:

- failure to reduce efficiently the parameter space (as already shown for the simplified basin-scale model of Section 2.2 and further illustrated in the  
575 Supplementary Material),

- overestimation of the influence of model parameters on the model response (see Fig. 2.2),
- requirement to assume a reference parameter set, which is highly subjective and dependent on prior knowledge,
- 580 • nearly identical calibrated parameter values as for the study without a SA (Tab. 1 in the Supplementary Material),
- impossibility to deduce potential deficiencies of underlying physical model, due to parameter insensitivity and untested areas of the parameter space.

To conclude, we need a global sensitivity analysis for the reduction of the parameter space to ensure a robust model calibration and to investigate possible parameter correlations. In this paper, we presented the two end-members of a local SA and a global Sobol SA. However, note that also analyses that combine aspects of both local and global SAs exist. One example is the Morris SA, which could address the reliance on the reference parameters (Campolongo et al. 2007; Morris, 1991; Wainwright et al. 2014). The Morris sensitivity analysis is difference-based, as the local sensitivity analysis. It requires fewer forward simulations than the Sobol sensitivity analysis. Therefore, it is computationally cheaper. In contrast to the Sobol sensitivity analysis, it does not allow an intensive study of the parameter correlations (Campolongo et al. 2007; Morris 1991; Wainwright et al. 2014). Since these correlations are of major interest in geothermal studies, we advise using the Sobol sensitivity analysis with a surrogate model to compensate for the computational costs.

#### *Geological Conclusion of the Sensitivity Analysis*

While our contribution focuses on methodology, it is also interesting to discuss some geological aspects from the results of the global SA.

Tendentiously, we obtain higher influences from the upper layers (see Section 3.4.3). This is expected since the measurements are located in these layers (the deepest measurement at about 5 km depth). The smaller influence from the

Cenozoic Volcanics (CV) can be attributed to upper boundary condition. At the  
605 top of the model, we applied indeed a Dirichlet Boundary condition, which fixes  
the temperatures to the regional average annual temperature values. Hence,  
the possible model variations in the uppermost part of the model are limited,  
which explains the resulting smaller sensitivities. The high influence from the  
Lithospheric Mantle (LM1 & LM2) can also partly be explained by its location,  
610 but it is mainly caused by the large layer thickness.

For the SA, we need to define a quantity of interest, which is tailored to the  
aims of further analyses. In our study, we want to perform a model calibration,  
which minimizes the difference between simulated and observed temperatures.  
Hence, our study is focused on the temperatures at the measurement locations.  
615 Consequently, we focus also our SAs on the measurements. Note that if we were  
interested in the physical processes, we would need to chose a different quantity  
of interest, such as the total amount of heat in the system, to avoid a potential  
measurement bias.

For our measurement-focused study, we find the influences of the radiogenic  
620 heat production to be negligible in comparison to the thermal conductivities.  
This is the reason why we did not account for these parameters in further  
analyses. The minor influence of the radiogenic heat production (the sensitivity  
index of the most influencing radiogenic heat production is nearly one order of  
magnitude smaller than the one of the thermal conductivity of the Cenozoic  
625 Rift Sediments (see Fig. 2 in the Supplementary Material)) is contradictory to  
the results from Freymark et al. (2017). The discrepancy is either caused by the  
choice of the sensitivity analysis (we used a global study in contrast to the local  
study from Freymark et al. (2017)) or different quantities of interest. In our case  
study, we chose the misfit to the temperature measurements as the quantity of  
630 interest. In contrast, Freymark et al. (2017) looked at the temperature changes  
inside the entire model. In the case of perfect data coverage, the results of  
both studies should be the same. However, we have many areas in the model  
where no temperature measurements are available. In our study, we investigated  
which thermal properties are influencing the temperatures at the measurement

635 locations since we calibrate the model with these measurements and found the  
radiogenic heat productions to be of low relevance. However, this does not  
mean that they are irrelevant for the understanding of the subsurface of the  
model region. A model only answers a specific question and investigating which  
thermal properties are influencing the entirety of the model would require a  
640 different study.

#### 4.2. Data Sparsity

One main difficulty of working with most observation data consists in dealing  
with very uneven spatial distributions. Note that this problem of data sparsity  
is a general one, not specific to the Upper Rhine Graben. A detailed analysis of  
645 how the SA is influenced by data sparsity is presented in [Degen et al. \(2021\)](#). We  
present here a way to compensate for the sparsity during the model calibration in  
general, using different data weighting strategies, along with some consequences  
for the Upper Rhine Graben in specifically.

As a reminder, for the geological model of Section [3](#) we have 2282 data  
650 points in region 1, 53 in region 2, and 12 data points in region 3 (Fig. [3.8](#)).  
Hence, region 1 contains one order of magnitude more data than region 2 and  
two orders of magnitude more data than region 3. Performing a calibration  
without applying any weights to the data reduces therefore mainly the misfit  
in region 1, only affecting slightly the misfits in regions 2 and 3, in line with  
655 the overall regions contributions. This can be seen in Fig. [3.8](#) by comparing  
the temperature values of the model calibration without weights and the initial  
temperature distribution. The difference between these two is insignificant,  
especially under consideration of the measurement accuracy. If we are only in-  
terested in region 1 of the model it is sufficient to follow the approach of a model  
660 calibration without any weights. However, this is not enough for a more even  
fit over the entire spatial domain. To compensate for the unequal distribution  
of observations, we apply user-defined weights to the different regions, as de-  
scribed in Section [3.2](#). This results in a slightly worse fit for region 1 compared  
to the initial temperature distribution. However, the misfit in region 2 can be

665 decreases significantly from 29 °C to 17 °C. The misfit in region 3 is comparable  
for both realizations.

The calibration with automatic weights yields very similar results to the  
calibration without weights. We explain this result by focussing on the spatial  
distribution of the misfit inside the southern and central part of the Upper Rhine  
670 Graben. In these areas, we can identify three zones: i) the central part with a  
zone of overall underestimated temperatures, as well as its ii) northern and iii)  
southern zones, both with overall overestimated temperatures. These zones of  
over- and underestimated temperatures correspond to region 2. Therefore, this  
is the region in which the conductive model fails to represent the measured tem-  
675 perature distribution. If we use the automated weighting scheme that considers  
distances only, we apply a higher weight to both the over- and underestimated  
temperature regions and we increase for both parts the contribution to the total  
misfit, which the calibration minimizes. The user-defined scheme only applies  
a higher weight to the overestimated temperature zones, therefore we increase  
680 the contribution to the total misfit of this region alone yielding the difference  
between those two schemes.

#### *Consequences of the Data Weighting Analysis for the Upper Rhine Graben Model*

Analogously to Section 4.1 on SAs, we draw several geological conclusions  
for the data weighting analysis. Using the model calibration with user-defined  
685 weights and a global SA (branch 1.3.3 of Fig. 3.3) leaves us with two param-  
eters that can be calibrated: the thermal conductivities of the Cenozoic Rift  
Sediments (CRS) and the Lithospheric Mantle (LM1 & LM2). This is in ac-  
cordance with our geological understanding of the model. In the case of the  
user-defined weights, we concentrate the calibration nearly exclusively on the  
690 area of the Upper Rhine Graben. As such, we can explain the mismatch of the  
temperature values in region 2 from the initial parameter distribution. However,  
if we focus our analysis on the Upper Rhine Graben itself, the calibration will  
be dominated by the dominant geological layer of the Upper Rhine Graben: the  
Cenozoic Rift Sediments (CRS). This is geologically plausible since a focus on

695 the Upper Rhine Graben should increase the importance of the layers inside the  
Grabens. Note that if we focus the model calibration on the entire model, we  
can also determine the behavior of other layers such as the Cenozoic Volcanics  
(CV).

700 For all model calibrations, we observe two regions of over-fitted temperature  
values and one region of under-fitted temperature values, all inside the Upper  
Rhine Graben. The boundary of this region correlates with the vertical bound-  
aries of the Variscan units, which indicates a possible error in the geometrical  
model, whose possible improvement is now identified and will be subject to  
future studies.

705 Overall, the spatial distribution of the misfit suggests that a conductive  
model is sufficient to describe the temperature distribution in the area outside  
the southern and central part of the Upper Rhine Graben. In the mentioned  
area, we observe a significant misfit to the observed temperatures and the cal-  
ibration with weights shows that this misfit is caused by an effect that leads  
710 to a decreased thermal conductivity in the Cenozoic Volcanics (CV) and Rift  
Sediments (CRS). Looking closer at this area in the literature, we find that  
especially the area of the central part of the Upper Rhine Graben is character-  
ized by highly permeable sediments with a dense fault network (Buchmann &  
Connolly, 2007; Bauer et al., 2015; Vidal & Genter, 2018; Meixner et al., 2016).  
715 Combining these structural characteristics with the discrepancy in the thermal  
conductivity of the upper two layers leads to the conclusion that the misfit might  
be related to fluid interactions and related effects on heat transport (such as  
convection). Both effects are ignored in the current conductive model, which  
does not consider any faults or fractures as it focuses on the temperature of at  
720 basin-scale. This conclusion is supported by Freymark et al. (2019), who show  
that these features become important for local studies and that the temperature  
discrepancy is a result of the advective heat transport.

In contrast to previous studies, we have identified the two layers that are  
responsible for the misfit and systematically determined which of these layers is  
725 of higher importance. Furthermore, based on the sensitivity analysis, we have

determined that most of these misfits are caused by the two layers themselves, and only a significantly smaller part is introduced by the correlation with other parameters.

### 4.3. Computational Cost

Table 2: Overview of the computational costs for the sensitivity analysis of both reduced models of the Upper Rhine Graben.

Model	FE simulation time [min]	Offline Stage [h]	Number of basis functions	Online time [s]	Speed-up	Global SA [s]	Local SA [s]
1. RB model	$2.64 \cdot 10^3$	$1.27 \cdot 10^5$	128	$3 \cdot 10^{-3}$	$9.2 \cdot 10^5$	$5 \cdot 10^2$	$5 \cdot 10^{-2}$
2. RB model	$2.64 \cdot 10^3$	$8.39 \cdot 10^4$	25	$1 \cdot 10^{-3}$	$2.7 \cdot 10^6$	$9 \cdot 10^1$	$1 \cdot 10^2$

730 The global SA was only made feasible by using highly efficient surrogate models with the RB method. Generating the RB model itself, however, has an initial computational cost, which is represented by the computation time of the offline stage (Tab. 2). The offline stage of the Upper Rhine Graben with varying thermal conductivities required 128 basis functions and took 35.7 h, 735 on an Intel Westmere X675 machine (3.07 GHz 6 cores per chip, 12 cores per node, and 24 GB memory per node) using 48 cores. The other offline stage, with varying radiogenic heat productions, required 25 basis functions yielding a total computation time of 23.3 h on the same machine. If we compare that to 740 that we are far more efficient with the reduced basis method than with the finite element method. Furthermore, the reduction is a one-time cost. So we can use the same reduced model for further investigations and do not require another time-consuming offline stage.

In the current stage, the RB method provides efficient error bounds only  
745 for elliptic and parabolic partial differential equations (PDE). For a geothermal  
application, this has the consequence that the method is only applicable to con-  
ductive studies if we want to obtain a guarantee for the approximation error.  
The RB method is also applicable for hyperbolic problems but in this case, we  
only obtain estimates of the approximation error. Also note, that we need to  
750 decompose the PDE into a parameter-dependent and -independent part. This  
is naturally given for linear problems, but not for nonlinear ones. Nonetheless,  
the method is also applicable for nonlinear PDEs by using the empirical inter-  
polation method (e.g. [Barrault et al. 2004](#)), which approximates the nonlinear  
part of the PDE.

## 755 5. Conclusion

We performed systematic geothermal model calibrations and sensitivity stud-  
ies, illustrating the methodological conclusions on a case study of the Upper  
Rhine Graben. We demonstrated the shortcomings of local sensitivity analysis,  
most commonly used as “trial-and-error” method, and showed that only the  
760 model calibration in combination with the global SA results in a robust and  
reliable model calibration. Additionally, we explained how a calibration based  
on global SAs can even identify errors in the underlying physical model, which  
serves as a prerequisite to possibly compensate for these errors at a later stage.  
Not only were we able to identify the spatial areas with model errors (arising,  
765 for instance, from unaccounted physical processes) but we furthermore quan-  
tified the influence of the thermal conductivity on these areas. As such, we  
showed that a simple conductive model can actually compensate for the errors  
in the underlying physics and potentially provide more reliable predictions tem-  
peratures at the target depth of geothermal exploration applications than more  
770 complex models accounting for all relevant physical processes.

Furthermore, we encountered in this study the problem of data sparsity,  
as in many geophysical applications. Through different weighting schemes, we

offered systematic methods to compensate for this sparsity during the analyses and therefore possibilities to reduce the bias caused by this unequal data  
775 distribution.

The combination of a global sensitivity study and an automated model calibration is computationally prohibitive with state-of-the-art finite element simulations for high-resolution models, like basin-scale geothermal models as investigated here. Therefore, we used the RB method as a surrogate model, for  
780 the inverse processes. This reduced the computation time from 36 core-years to 10 core-minutes plus the initial cost of the generation of the surrogate model, leading to a speed-up of several orders of magnitude. On top of this, the surrogate model can be re-used for other analyses. This makes the method extremely promising to identify model discrepancy and to determine the dominant model  
785 parameters, as we illustrated with novel geological conclusions reached about the Upper Rhine Graben.

Our results on this case study open up the path to several subsequent steps. We showed that the calibration indicates the need to consider the fluid interaction in the upper layers. Due to the high dimensionality of the model, a  
790 hydrothermal simulation becomes computationally very costly, making global sensitivity analyses as investigated here prohibitively expensive. Furthermore, the number of parameters that need to be calibrated increases, making a calibration of the individual parameters increasingly difficult, due to the data sparsity (Freymark et al. 2019). In order to perform both efficient inverse processes and  
795 consider the hydrothermal effects, novel approaches will be required to introduce another step change, using potentially concepts such as the entropy production (Börsing et al. 2017; Huang & Wellmann 2021), to transfer the effects of the convection into effective thermal conductivities.

### Acknowledgement

800 We would like to acknowledge the funding provided by the DFG through DFG Project GSC111. We also gratefully acknowledge the computing time

granted through JARA-HPC on the supercomputer JURECA at Forschungszentrum Jülich. This is a pre-print of an article published in Geothermics. The final authenticated version is available online at: <https://doi.org/10.1016/j.geothermics.2021.102143>

805 **References**

- Agemar, T., Brunken, J., Jodocy, M., Schellschmidt, R., Schulz, R., & Stober, I. (2013). Untergrundtemperaturen in Baden-Württemberg. *Zeitschrift der Deutschen Gesellschaft für Geowissenschaften*, *164*, 49–62.
- Agemar, T., Weber, J., & Schulz, R. (2014). Deep geothermal energy production  
810 in Germany. *Energies*, *7*, 4397–4416.
- Baroni, G., & Tarantola, S. (2014). A General Probabilistic Framework for uncertainty and global sensitivity analysis of deterministic models: A hydrological case study. *Environmental Modelling & Software*, *51*, 26–34.
- Barrault, M., Maday, Y., Nguyen, N. C., & Patera, A. T. (2004). An empirical  
815 interpolation method: application to efficient reduced-basis discretization of partial differential equations. *Comptes Rendus Mathématique*, *339*, 667–672.
- Bauer, J. F., Meier, S., & Philipp, S. L. (2015). Architecture, fracture system, mechanical properties and permeability structure of a fault zone in Lower Triassic sandstone, Upper Rhine Graben. *Tectonophysics*, *647*, 132–145.
- 820 Bayer, U., Scheck, M., & Koehler, M. (1997). Modeling of the 3D thermal field in the northeast German basin. *Geologische Rundschau*, *86*, 241–251.
- Börsing, N., Wellmann, J. F., Niederau, J., & Regenauer-Lieb, K. (2017). Entropy production in a box: Analysis of instabilities in confined hydrothermal systems. *Water Resources Research*, *53*, 7716–7739.
- 825 Branch, M. A., Coleman, T. F., & Li, Y. (1999). A subspace, interior, and conjugate gradient method for large-scale bound-constrained minimization problems. *SIAM Journal on Scientific Computing*, *21*, 1–23.

- Buchmann, T. J., & Connolly, P. T. (2007). Contemporary kinematics of the Upper Rhine Graben: a 3D finite element approach. *Global and Planetary Change*, *58*, 287–309.
- 830
- Byrd, R. H., Schnabel, R. B., & Shultz, G. A. (1988). Approximate solution of the trust region problem by minimization over two-dimensional subspaces. *Mathematical programming*, *40*, 247–263.
- Cacace, M., Blöcher, G., Watanabe, N., Moeck, I., Börsing, N., Scheck-Wenderoth, M., Kolditz, O., & Huenges, E. (2013). Modelling of fractured carbonate reservoirs: outline of a novel technique via a case study from the Molasse Basin, southern Bavaria, Germany. *Environmental earth sciences*, *70*, 3585–3602.
- 835
- Campolongo, F., Cariboni, J., & Saltelli, A. (2007). An effective screening design for sensitivity analysis of large models. *Environmental modelling & software*, *22*, 1509–1518.
- 840
- Cannavó, F. (2012). Sensitivity analysis for volcanic source modeling quality assessment and model selection. *Computers & geosciences*, *44*, 52–59.
- Cloke, H., Pappenberger, F., & Renaud, J.-P. (2008). Multi-method global sensitivity analysis (MMGSA) for modelling floodplain hydrological processes. *Hydrological Processes: An International Journal*, *22*, 1660–1674.
- 845
- Degen, D., Spooner, C., Scheck-Wenderoth, M., & Cacace, M. (2021). How biased are our models? – A Case Study of the Alpine Region. *Geoscientific Model Development Discussions (submitted)*.
- 850
- Degen, D., Veroy, K., & Wellmann, F. (2020). Certified reduced basis method in geosciences. *Computational Geosciences*, *24*, 241–259.
- Deutscher Wetterdienst (2020). Climate monitoring Germany. [https://www.dwd.de/EN/climate\\_environment/climate\\_monitoring/germany/germany\\_node.html](https://www.dwd.de/EN/climate_environment/climate_monitoring/germany/germany_node.html)

- 855 Fernández, M., Eguía, P., Granada, E., & Febrero, L. (2017). Sensitivity analysis  
of a vertical geothermal heat exchanger dynamic simulation: Calibration and  
error determination. *Geothermics*, *70*, 249–259.
- Freyemark, J., Bott, J., Cacace, M., Ziegler, M., & Scheck-Wenderoth, M. (2019).  
Influence of the Main Border Faults on the 3D Hydraulic Field of the Central  
860 Upper Rhine Graben. *Geofluids*, *2019*.
- Freyemark, J., Sippel, J., Scheck-Wenderoth, M., Bär, K., Stiller, M., Fritsche,  
J.-G., & Kracht, M. (2017). The deep thermal field of the Upper Rhine  
Graben. *Tectonophysics*, *694*, 114–129.
- Geem, Z. W. (2012). *Optimization in Civil & Environmental Engineering*.  
865 Archives contemporaines.
- GeORG-Projektteam (2013). Geopotenziale des tieferen Untergrundes im Ober-  
rheingraben. *Fachlich- Technischer Abschlussbericht des INTERREG- Pro-  
jekts GeORG, Teil 1, LGRB-Informationen*, *28*, 1–104.
- Geothermie, P. T. (2007). Nutzungen der geothermischen energie aus dem tiefen  
870 Untergrund (tiefe Geothermie)–arbeitshilfe für Geologische Dienste.
- Golberg, D. E. (1989). Genetic algorithms in search, optimization, and machine  
learning. *Addion wesley*, *1989*, 36.
- van Griensven, A. v., Meixner, T., Grunwald, S., Bishop, T., Diluzio, M., &  
Srinivasan, R. (2006). A global sensitivity analysis tool for the parameters of  
875 multi-variable catchment models. *Journal of hydrology*, *324*, 10–23.
- Grimmer, J., Ritter, J., Eisbacher, G., & Fielitz, W. (2017). The Late Variscan  
control on the location and asymmetry of the Upper Rhine Graben. *Interna-  
tional Journal of Earth Sciences*, *106*, 827–853.
- Herman, J., & Usher, W. (2017). Salib: an open-source python library for  
880 sensitivity analysis. *J. Open Source Softw*, *2*, 97.

- Hesthaven, J. S., Rozza, G., Stamm, B. et al. (2016). *Certified reduced basis methods for parametrized partial differential equations*. SpringerBriefs in Mathematics, Springer.
- Houghton, J. T., Ding, Y., Griggs, D. J., Noguera, M., van der Linden, P. J., Dai,  
885 X., Maskell, K., & Johnson, C. (2001). *Climate change 2001: the scientific basis*. The Press Syndicate of the University of Cambridge.
- Huang, P.-W., & Wellmann, F. (2021). An explanation to the nusselt-rayleigh discrepancy in naturally convected porous media. *Transport in Porous Media*, 137(1), 195–214.
- 890 Illies, J. (1972). The Rhine graben rift system-plate tectonics and transform faulting. *Geophysical surveys*, 1, 27–60.
- Kolditz, O., & Clauser, C. (1998). Numerical simulation of flow and heat transfer in fractured crystalline rocks: application to the hot dry rock site in Rosemanowes (UK). *Geothermics*, 27, 1–23.
- 895 Konrad, F., Savvatis, A., Wellmann, F., & Zosseder, K. (2019). Hydraulic behavior of fault zones in pump tests of geothermal wells: a parametric analysis using numerical simulations for the Upper Jurassic aquifer of the North Alpine Foreland Basin. *Geothermal Energy*, 7, 1–28.
- Lehmann, H., Wang, K., & Clauser, C. (1998). Parameter identification and  
900 uncertainty analysis for heat transfer at the KTB drill site using a 2-D inverse method. *Tectonophysics*, 291, 179–194.
- Meixner, J., Schill, E., Grimmer, J. C., Gaucher, E., Kohl, T., & Klingler, P. (2016). Structural control of geothermal reservoirs in extensional tectonic settings: an example from the Upper Rhine Graben. *Journal of Structural  
905 Geology*, 82, 1–15.
- Morris, M. D. (1991). Factorial sampling plans for preliminary computational experiments. *Technometrics*, 33, 161–174.

- Murphy, J. M., Sexton, D. M., Barnett, D. N., Jones, G. S., Webb, M. J., Collins, M., & Stainforth, D. A. (2004). Quantification of modelling uncertainties in  
910 a large ensemble of climate change simulations. *Nature*, *430*, 768–772.
- Pauwels, H., Fouillac, C., & Fouillac, A.-M. (1993). Chemistry and isotopes of deep geothermal saline fluids in the Upper Rhine Graben: Origin of compounds and water-rock interactions. *Geochimica et Cosmochimica Acta*, *57*, 2737–2749.
- 915 Prud’homme, C., Rovas, D. V., Veroy, K., Machiels, L., Maday, Y., Patera, A. T., & Turinici, G. (2002). Reliable real-time solution of parametrized partial differential equations: Reduced-basis output bound methods. *Journal of Fluids Engineering*, *124*, 70–80.
- Quarteroni, A., Manzoni, A., & Negri, F. (2015). *Reduced Basis Methods for Partial Differential Equations: An Introduction*. UNITEXT. Springer International Publishing.
- Randolph, J. B., & Saar, M. O. (2011). Combining geothermal energy capture with geologic carbon dioxide sequestration. *Geophysical Research Letters*, *38*.
- Ray, S., Mukherjee, J., & Mandal, S. (2015). Modelling nitrogen and carbon  
925 cycles in Hooghly estuary along with adjacent mangrove ecosystem. In *Developments in Environmental Modelling* (pp. 289–320). Elsevier volume 27.
- Refsgaard, J. C., van der Sluijs, J. P., Højberg, A. L., & Vanrolleghem, P. A. (2007). Uncertainty in the environmental modelling process—a framework and guidance. *Environmental modelling & software*, *22*, 1543–1556.
- 930 Saltelli, A. (2002). Making best use of model evaluations to compute sensitivity indices. *Computer physics communications*, *145*, 280–297.
- Saltelli, A., Annoni, P., Azzini, I., Campolongo, F., Ratto, M., & Tarantola, S. (2010). Variance based sensitivity analysis of model output. Design and estimator for the total sensitivity index. *Computer Physics Communications*,  
935 *181*, 259–270.

- Saltelli, A., Tarantola, S., Campolongo, F., & Ratto, M. (2004). Sensitivity analysis in practice: a guide to assessing scientific models. *Chichester, England*, .
- Sobol, I. M. (2001). Global sensitivity indices for nonlinear mathematical models and their Monte Carlo estimates. *Mathematics and computers in simulation*, 940 55, 271–280.
- Song, X., Zhang, J., Zhan, C., Xuan, Y., Ye, M., & Xu, C. (2015). Global sensitivity analysis in hydrological modeling: Review of concepts, methods, theoretical framework, and applications. *Journal of hydrology*, 523, 739–757.
- 945 Stober, I., & Bucher, K. (2015). Hydraulic and hydrochemical properties of deep sedimentary reservoirs of the Upper Rhine Graben, Europe. *Geofluids*, 15, 464–482.
- Tang, Y., Reed, P., Van Werkhoven, K., & Wagener, T. (2007). Advancing the identification and evaluation of distributed rainfall-runoff models using global sensitivity analysis. *Water Resources Research*, 43.
- 950 Turcotte, D. L., & Schubert, G. (2002). *Geodynamics*. Cambridge university press.
- Vidal, J., & Genter, A. (2018). Overview of naturally permeable fractured reservoirs in the central and southern Upper Rhine Graben: Insights from geothermal wells. *Geothermics*, 74, 57–73.
- 955 Vidal, J., Genter, A., Schmittbuhl, J., Whitechurch, H., Baujard, C., & Damalais, E. (2015). Evolution of concepts for the geothermal projects in the Upper Rhine Graben. In *European Geothermal Workshop, Strasbourg, France*.
- 960 Virtanen, P., Gommers, R., Oliphant, T., Travis, E., Haberland, M., Reddy, T., Cournapeau, D., Burovski, E., Peterson, P., Weckesser, W. & Bright, J. (2020). SciPy 1.0: fundamental algorithms for scientific computing in Python. *Nature methods*, 17(3), 261–272.

- Vogt, C., Mottaghy, D., Wolf, A., Rath, V., Pechnig, R., & Clauser, C. (2010).  
965 Reducing temperature uncertainties by stochastic geothermal reservoir mod-  
elling. *Geophysical Journal International*, *181*, 321–333.
- Wagner, R., & Clauser, C. (2005). Evaluating thermal response tests using  
parameter estimation for thermal conductivity and thermal capacity. *Journal  
of Geophysics and Engineering*, *2*, 349–356.
- 970 Wainwright, H. M., Finsterle, S., Jung, Y., Zhou, Q., & Birkholzer, J. T. (2014).  
Making sense of global sensitivity analyses. *Computers & Geosciences*, *65*,  
84–94.
- Wellmann, F., & Caumon, G. (2018). 3-D Structural geological models: Con-  
cepts, methods, and uncertainties. *Advances in Geophysics*, *59*, 1–121.
- 975 Zhan, C.-S., Song, X.-M., Xia, J., & Tong, C. (2013). An efficient integrated  
approach for global sensitivity analysis of hydrological model parameters. *En-  
vironmental Modelling & Software*, *41*, 39–52.

# Supplementary Material for Global Sensitivity Analysis to Optimize Basin-Scale Conductive Model Calibration – A Case Study From the Upper Rhine Graben

Denise Degen<sup>a,\*</sup>, Karen Veroy<sup>b,c</sup>, Jessica Freyemark<sup>d,e</sup>, Magdalena  
Scheck-Wenderoth<sup>d,e</sup>, Thomas Poulet<sup>f</sup>, Florian Wellmann<sup>a</sup>

<sup>a</sup>*Computational Geoscience and Reservoir Engineering (CGRE), RWTH Aachen  
University, Wüllnerstraße 2, 52072 Aachen, Germany*

<sup>b</sup>*Centre for Analysis, Scientific Computing and Applications, Department of Mathematics  
& Computer Science, Eindhoven University of Technology (TU/e), Groene Loper 5,  
Eindhoven, The Netherlands*

<sup>c</sup>*Faculty of Civil Engineering, RWTH Aachen University, Schinkelstraße 2, Aachen,  
Germany*

<sup>d</sup>*GFZ German Research Centre for Geosciences, Telegrafenberg, 14473 Potsdam, Germany*

<sup>e</sup>*Department of Geology, Geochemistry of Petroleum and Coal, RWTH Aachen University,  
Aachen, Germany*

<sup>f</sup>*CSIRO Mineral Resources, Kensington, Western Australia*

---

---

In the main part of this article, we provided the general conclusions that can be drawn from the model of the Upper Rhine Graben. In this Supplementary Material, we provide all detailed results of the analyses, for completion, in form of tables and overview graphs.

## 5 Model Calibration without Sensitivity Analysis

Analogous to the article, we start the presentation of the results with the model calibration without a sensitivity analysis. Therefore, we present in Tab. **I** the initial thermal conductivities, as well as the calibrated thermal conductivities for all layers and all weighting schemes, i.e. for the i) no weights, ii) automatic weights, and iii) user-defined weights scenario. We also present the radiogenic heat production values. Note that the values were not varied in the calibration since the sensitivity analyses showed that the influence of the radiogenic heat production is minor in comparison to the thermal conductivity.

---

\*Corresponding author

We observe in Tab. 1 a high decrease in the thermal conductivity of the Cenozoic Rift Sediments (CRS) in case of the model calibration with user-defined weights with a decrease of  $0.4 \text{ W m}^{-1} \text{ K}^{-1}$ . Also, we obtain a high increase in thermal conductivity of  $0.9 \text{ W m}^{-1} \text{ K}^{-1}$  for the Cenozoic Volcanics (CV) for the model calibration without and with automatic weights.

Table 1: The thermal properties before and after the calibration for the Upper Rhine Graben without considering the results of a sensitivity study. The initial thermal conductivities  $\lambda_{\text{init}}$  and the radiogenic heat productions  $S$  are taken from Freyemark et al. (2017). We denote the training parameters with  $\mu$ , the calibrated thermal conductivities with  $\lambda_{\text{cal}}$ , and all parameters that are not involved in the model calibration, due to too low sensitivities, with n/a. Note that UC stands for Upper Crust.

ID	Layer	$\mu$	$\lambda_{\text{init}}$ [ $\text{W m}^{-1} \text{ K}^{-1}$ ]	$\lambda_{\text{cal}}$ [ $\text{W m}^{-1} \text{ K}^{-1}$ ]			$S$ [ $\mu\text{Wm}^{-3}$ ]
				no weights	automatic weights	user-defined weights	
CV	Cenozoic Volcanics	0	1.8	2.7 (ub)	2.7 (ub)	1.6	0.2
CRS	Cenozoic Rift Sediments	1	1.2	1.4	1.4	0.8	1.0
TS	Tertiary salt	2	6.0	5.5 (lb)	5.5 (lb)	5.5 (lb)	0.0
A	Alps	3	2.2	1.5	1.4	1.3	0.3
CM	Cenozoic Folded Molasse	4	3.0	3.5	3.4	4.5 (ub)	1.0
CFM	Cenozoic Foreland Molasse	4	3.0	3.5	3.4	4.5 (ub)	1.0
C	Cretaceous	3	2.2	1.5	1.4	1.3	0.5
M	Malm	5	2.7	2.8 (ub)	2.8 (ub)	2.8 (ub)	1.4
DLK	Dogger/Lias/Keuper	6	2.5	3.5 (ub)	3.2	2.4 (lb)	1.6
MK	Muschelkalk	7	2.0	1.5	2.1	3.0 (ub)	1.2
B	Buntsandstein	4	3.0	3.5	3.4	4.5 (ub)	1.0
Z	Zechstein	8	2.3	3.4 (ub)	3.4 (ub)	2.5	0.8
PC	Permo-Carboniferous	3	2.2	1.5	1.4	1.3	1.0
JM	Jura Mountains	4	3.0	3.5	3.4	4.5 (ub)	0.5
S	UC: Saxothuringian	6	2.5	3.5 (ub)	3.2	2.4 (lb)	2.5
O	UC: Odenwald	4	3.0	3.5	3.4	4.5 (ub)	1.8
MCH	UC: Mid-German Crystalline High	9	2.4	2.3 (lb)	2.3 (lb)	2.7 (ub)	1.8
NPZ	UC: Northern Phyllite Zone	5	2.7	2.8 (ub)	2.8 (ub)	2.8 (ub)	3.0
R	UC: Rhenohercynian	5	2.7	2.8 (ub)	2.8 (ub)	2.8 (ub)	1.0
MN	UC: Moldanubian	6	2.5	3.5 (ub)	3.2	2.4 (lb)	2.6
UC-A	UC: Alps	8	2.3	3.4 (ub)	3.4 (ub)	2.5	2.4
LC	Lower Crust	10	2.1	2.1 (lb)	2.3	2.1 (lb)	0.5
LM1	Lithospheric Mantle 1	11	3.95	5.9 (ub)	5.9 (ub)	4.1	0.03
LM2	Lithospheric Mantle 2	11	3.95	5.9 (ub)	5.9 (ub)	4.1	0.03

## Model Calibration with Local Sensitivity Analysis

20 In the following, we present how the calibrated values change by including the results of a local sensitivity study into the process of model calibration. The results of the local sensitivity analysis for the unweighted, automatic weighted, and user-defined weighted case are presented in Fig. 3.4. Here, we present the additional analysis performed for determining the influence of the radiogenic heat production. For this analysis, we compared in Fig. 1 the influences of the radiogenic heat productions of the Upper Crust and the thermal conductivity of the Cenozoic Rift Sediments (CRS).

The highest influence of the radiogenic heat production is arising from the Saxothuringian (S). However, the influence is significantly lower than the influence of the thermal conductivity of the Cenozoic Rift Sediments (CRS). This is the reason why we did not consider the radiogenic heat production during the model calibration.

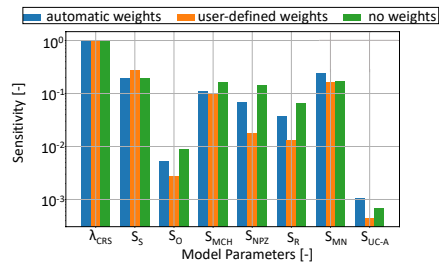


Figure 1: Local sensitivity analysis, for the reduced order model varying the thermal conductivity of the Cenozoic Rift Sediments and the radiogenic heat productions of the Upper Crust. The acronyms for the respective geological layers are defined in Tab. 1

As before, we present the detailed result of the calibration of the thermal conductivities, along with the initial values of the thermal conductivities and radiogenic heat productions, for all layers in Tab. 2

As discussed in the main article, the model calibration results without and with a local SA are alike (Tab. 2). Only for the Lower Crust (LC) and the Lithospheric Mantle (LM1 & LM2), differences are observed. We still, observe that many of the model parameters reach their upper or lower bound.

Table 2: The thermal properties before and after the calibration for the Upper Rhine Graben considering the results of the local sensitivity study. The initial thermal conductivities  $\lambda_{\text{init}}$  and the radiogenic heat productions  $S$  are taken from [Freymark et al. \(2017\)](#). We denote the training parameters with  $\mu$ , the calibrated thermal conductivities with  $\lambda_{\text{cal}}$ , and all parameters that are not involved in the model calibration, due to too low sensitivities, with n/a. Note that UC stands for Upper Crust.

ID	Layer	$\mu$	$\lambda_{\text{init}}$ [W m <sup>-1</sup> K <sup>-1</sup> ]	$\lambda_{\text{cal}}$ [W m <sup>-1</sup> K <sup>-1</sup> ]			S [ $\mu\text{Wm}^{-3}$ ]
				no weights	automatic weights	user-defined weights	
CV	Cenozoic Volcanics	0	1.8	2.7 (ub)	n/a	n/a	0.2
CRS	Cenozoic Rift Sediments	1	1.2	1.4	1.4	0.8	1.0
CM	Cenozoic Folded Molasse	4	3.0	3.3	3.3	4.5 (ub)	1.0
CFM	Cenozoic Foreland Molasse	4	3.0	3.3	3.3	4.5 (ub)	1.0
M	Malm	5	2.7	2.8 (ub)	2.8 (ub)	n/a	1.4
DLK	Dogger/Lias/Keuper	6	2.5	3.5 (ub)	3.2	2.4 (lb)	1.6
B	Buntsandstein	4	3.0	3.3	3.3	4.5 (ub)	1.0
JM	Jura Mountains	4	3.0	3.3	3.3	4.5 (ub)	0.5
S	UC: Saxothuringian	6	2.5	3.5 (ub)	3.2	2.4 (lb)	2.5
O	UC: Odenwald	4	3.0	3.3	3.3	4.5 (ub)	1.8
MCH	UC: Mid-German Crystalline High	9	2.4	2.3 (lb)	2.3 (lb)	2.7 (ub)	1.8
NPZ	UC: Nothern Phyllite Zone	5	2.7	2.8 (ub)	2.8 (ub)	n/a	3.0
R	UC: Rhenohercynian	5	2.7	2.8 (ub)	2.8 (ub)	n/a	1.0
MN	UC: Moldanubian	6	2.5	3.5 (ub)	3.2	2.4 (lb)	2.6
LC	Lower Crust	10	2.1	2.1 (lb)	2.6	2.1 (lb)	0.5
LM1	Lithospheric Mantle 1	11	3.95	5.9 (ub)	5.9 (ub)	4.3	0.03
LM2	Lithospheric Mantle 2	11	3.95	5.9 (ub)	5.9 (ub)	4.3	0.03

40 **Model Calibration with Global Sensitivity Analysis**

The global sensitivity analysis whose results are accounted for in the model calibration is presented in Fig. 3.6. Here, we present the comparison between the influences between the radiogenic heat productions of the Upper Crust and the thermal conductivity of the Cenozoic Rift Sediments (CRS) in Fig. 2. As for the local SA, we conclude that the highest influence of the radiogenic heat production is caused by the Saxothuringian (S). Since this influence is significantly lower than the one of the thermal conductivity of the Cenozoic Rift Sediments (CRS), we disregard the radiogenic heat productions during the calibration.

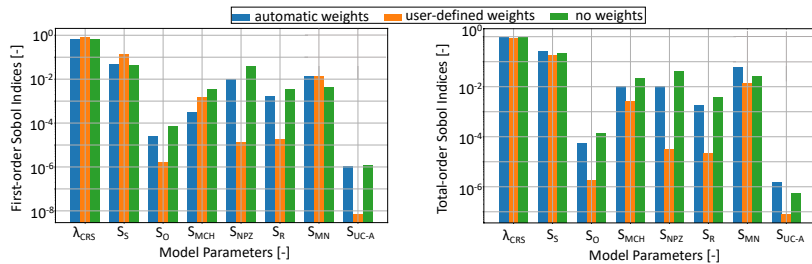


Figure 2: Comparison of the first and total order sensitivity-indices of the global sensitivity analyses for the second reduced model of the Upper Rhine Graben model. The acronyms for the respective geological layers are defined in Tab. 1

Tab. 3 contains the initial thermal properties (thermal conductivity and radiogenic heat production), and the calibrated thermal conductivities of all layers for all weighting schemes.

Regarding the calibration without weights (branch 1.1.3 of Fig. 3.3), we observe, for the Cenozoic Volcanics (CV) and Rift Sediments (CRS) and the Lithospheric Mantle (LM1 & LM2), an increase in thermal conductivity in contrast to the initial thermal conductivities. This yields thermal conductivities of  $2.4 \text{ W m}^{-1} \text{ K}^{-1}$ ,  $1.3 \text{ W m}^{-1} \text{ K}^{-1}$ , and  $4.9 \text{ W m}^{-1} \text{ K}^{-1}$ , respectively. The Cenozoic Folded Molasse (CM)/Cenozoic Foreland Molasse (CFM)/Buntsandstein/(B)Jura Mountains (JM)/Odenwald (O) layers have a thermal conductivity of  $3.0 \text{ W m}^{-1} \text{ K}^{-1}$ , the same value before and after the calibration with automatic weights (branch 1.2.3 of Fig. 3.3) yields similar thermal

conductivities as the one without weights.

For the calibration with user-defined weights (branch 1.3.3 of Fig. 3.3), we observe for the Rift Sediments (CRS) a decrease in thermal conductivity after the calibration, resulting in an extremely low thermal conductivity of  $0.8 \text{ W m}^{-1} \text{ K}^{-1}$ . The Lithospheric Mantle (LM1 & LM2) has a slightly decreased thermal conductivity of  $3.6 \text{ W m}^{-1} \text{ K}^{-1}$  in contrast to the initial thermal conductivity of  $3.95 \text{ W m}^{-1} \text{ K}^{-1}$ .

Table 3: The thermal properties before and after the calibration for the Upper Rhine Graben considering the results of the global sensitivity study. The initial thermal conductivities  $\lambda_{\text{init}}$  and the radiogenic heat productions  $S$  are taken from [Freymark et al., \(2017\)](#). We denote the training parameters with  $\mu$ , the calibrated thermal conductivities with  $\lambda_{\text{cal}}$ , and all parameters that are not involved in the model calibration, due to too low sensitivities, with n/a. Note that UC stands for Upper Crust.

ID	Layer	$\mu$	$\lambda_{\text{init}}$ [ $\text{W m}^{-1} \text{ K}^{-1}$ ]	$\lambda_{\text{cal}}$ [ $\text{W m}^{-1} \text{ K}^{-1}$ ]			S [ $\mu\text{W m}^{-3}$ ]
				no weights	automatic weights	user-defined weights	
CV	Cenozoic Volcanics	0	1.8	2.4	2.6	n/a	0.2
CRS	Cenozoic Rift Sediments	1	1.2	1.3	1.3	0.8	1.0
CM	Cenozoic Folded Molasse	4	3.0	3.0	2.9	n/a	1.0
CFM	Cenozoic Foreland Molasse	4	3.0	3.0	2.9	n/a	1.0
B	Buntsandstein	4	3.0	3.0	2.9	n/a	1.0
JM	Jura Mountains	4	3.0	3.0	2.9	n/a	0.5
O	UC: Odenwald	4	3.0	3.0	2.9	n/a	1.8
LM1	Lithospheric Mantle 1	11	3.95	4.9	5.2	3.6	0.03
LM2	Lithospheric Mantle 2	11	3.95	4.9	5.2	3.6	0.03

## Robustness

We investigate the robustness of the model calibrations without weights and  
70 with user-defined weights (branches 1.1.1 to 1.1.3, to 1.3.1 to 1.3.3 of Fig. 3.3) by  
decreasing the allowed variation range from  $\pm 50\%$  to  $\pm 10\%$  in step sizes of  $10\%$ .  
For this analysis, only the model calibration with a global sensitivity analysis  
behaves in accordance with our expectations. Both the model calibration with-  
out a sensitivity study and with a local sensitivity study behave nonphysically.  
75 For example, if we define a variation range of  $\pm 10\%$  the thermal conductivity of  
the Cenozoic Folded Molasse/Cenozoic Foreland Molasse/Buntsandstein/Jura  
Mountains/Odenwald layers decreases to its lower bound of  $2.7 \text{ W m}^{-1} \text{ K}^{-1}$ .  
Note that the initial value is  $3.0 \text{ W m}^{-1} \text{ K}^{-1}$ . However, if we now increase the  
variation range to  $\pm 20\%$ , then the thermal conductivity increases to its upper  
80 bound of  $3.6 \text{ W m}^{-1} \text{ K}^{-1}$ , which is physically not plausible.

In order to control the robustness of the different model calibration versions,  
we performed the model calibration without a sensitivity study, with a local sen-  
sitivity study, and with a global sensitivity study with different initial guesses.  
All model calibrations are tested using the user-defined weights (branches 1.3.1  
85 to 1.3.3 of Fig. 3.3). We tested the parameter values provided by [Frey](#)  
[et al. \(2017\)](#) as an initial guess, the lower and upper parameter bounds, and ten  
randomly chosen initial parameter sets. The least robust model calibration is  
the one without a sensitivity analysis (branch 1.3.1 of Fig. 3.3).  
It shows the highest differences with thermal conductivity differences in the  
90 order of  $10^{-2} \text{ W m}^{-1} \text{ K}^{-1}$ .

The model calibration with a local sensitivity analysis (branch 1.3.2 of Fig.  
3.3) yields differences in the order of  $10^{-5} \text{ W m}^{-1} \text{ K}^{-1}$ , and the one with a global  
sensitivity (branch 1.3.3 of Fig. 3.3) difference in the order of  $10^{-4} \text{ W m}^{-1} \text{ K}^{-1}$ .  
Hence, a first conclusion might be that both the model calibrations with the  
95 local and the global sensitivity study result in robust model calibrations since  
they converge to the same results.

However, if we look a bit closer at the model calibration with the local sen-



analysis fails to efficiently reduce the parameter space. This means we remain  
with insensitive parameters in the model calibration. These parameters cause  
110 the non-robustness since any for these parameters any value results in the same  
temperature distribution.

## References

Freymark, J., Sippel, J., Scheck-Wenderoth, M., Bär, K., Stiller, M., Fritsche,  
J.-G., & Kracht, M. (2017). The deep thermal field of the Upper Rhine  
115 Graben. *Tectonophysics*, *694*, 114–129.